




FACULTY OF SCIENCE AND TECHNOLOGY

MASTER'S THESIS

Study programme / specialisation: Marine and Offshore Technology	The spring semester, 2023 Open / Confidential
Author: Gorikhin Alexandr	 (signature author)
Supervisors at UiS: Prof. Muk Chen Ong, Dr. Guang Yin External supervisor: Christian Olsen	
Thesis title: Suction effect of skirted mud mat of GRP covers under wave loads	
Credits (ECTS): 30	
Keywords: Wave-structure-seabed interaction, Skirted GRP, Momentary liquefaction, CFD	Pages:42 + appendix:.....0..... Stavanger, ...14/05/202.....

Abstract

To mitigate potential risks of soil and structural failures in offshore foundation systems, it is crucial to examine seabed soil behavior near the structure especially near the skirtfaces under dynamic wave loads. This research aims to analyze wave-induced soil response and liquefaction risk in the vicinity of an offshore skirted GRP cover. A two-dimensional (2D) numerical analysis is performed using an integrated multiphysics model, implemented in the finite volume method (FVM) based on OpenFOAM framework. Nonlinear waves and anisotropic poro-elastic seabed soil solvers are included in the model. Such parameters as a wave elevation, total soil pore pressure, lifting force (F_z) and drag force (F_x) were verified through grid convergence studies. A parametric study with different wave heights and KC number was realized.

The objective of this study is to explore the dispersion of total (wave- and structure-induced) pore pressure, vertical displacement, pressure gradient, vertical effective stress, shear stress and seepage flow. The results indicate that the liquefaction mostly occurs along the internal skirtfaces and depends on the skirts length. The most severe liquefaction rates are at the moment when wave crest or wave trough is passing the construction. Due to the high initial effective stress the momentary liquefaction at the structure bottom center is insignificant.

Acknowledgments

This thesis marks the end of my master's degree in Marine and Offshore Technology at the University of Stavanger (UiS).

I am deeply grateful to Professor Muk Chen Ong, my supervisor, for providing me with the opportunity to explore the presented thesis topic. Professor Ong is devoted to his students and actively seeks ways to enhance their learning experience, for which I am thankful to have been a part of.

I would also like to express my gratitude to Dr. Guang Yin, my co-supervisor, for his exceptional guidance and support throughout my thesis work. Dr. Yin's expertise and selflessness have been tremendously beneficial during all stages of my research.

I also extend my appreciation to Christian Olsen, my external supervisor, for providing real case topic and referenced information.

Lastly, I extend my thanks to the Department of Mechanical and Structural Engineering and Materials Science at UiS for providing me with the necessary infrastructure to conduct my research.

Contents

Abstract	Error! Bookmark not defined.
Acknowledgments.....	Error! Bookmark not defined.
1. Introduction.....	Error! Bookmark not defined.
2. Theoretical background	Error! Bookmark not defined.
2.1. Skirted GRP covers	Error! Bookmark not defined.
2.2. Free Surface Wave Model.....	Error! Bookmark not defined.
2.3 Isotropic Poro-Elastic Soil Model	Error! Bookmark not defined.
2.4 Finite volume method based approach	Error! Bookmark not defined.
2.5 Keulegan-Carpenter Number	Error! Bookmark not defined.
3 Boundary Coupling Algorithm	Error! Bookmark not defined.
4 Model Validation	Error! Bookmark not defined.
5 Model Application	Error! Bookmark not defined.
5.1 Wave domain settings.....	Error! Bookmark not defined.
5.2 Seabed Domain Settings	Error! Bookmark not defined.
6 Convergence studies.....	Error! Bookmark not defined.
6.1 Wave Calibration.....	Error! Bookmark not defined.
6.2 Grid Convergence for Lifting Force (F_z) and Drag Force (F_x).....	Error! Bookmark not defined.
6.3 Grid Convergence study for Seabed Pore Pressure	Error! Bookmark not defined.
7 Results and discussion.....	Error! Bookmark not defined.
7.1 Consolidation	Error! Bookmark not defined.
7.2 Wave-Induced and Structure-Induced Seabed Responses ...	Error! Bookmark not defined.
7.3 Parametric study	Error! Bookmark not defined.
7.4 Parameters comparison with different wave heights	Error! Bookmark not defined.
7.5 Liquefaction Analysis	Error! Bookmark not defined.
8 Conclusions.....	Error! Bookmark not defined.
References	Error! Bookmark not defined.

List of figures

Figure 2.1.1 Skirted GRP Cover	8
Figure 3.1 Boundary coupling algorithm of wave-structure-seabed interaction.....	14
Figure 5.1 Illustration of the wave-structure-seabed interaction.....	15
Figure 5.2 Geometry parameters of the skirted GRP cover in the 2D. Skirt length 30 cm	Error! Bookmark not defined.
Figure 5.1.1 sketch of the numerical layout for the wave-structure-seabed interaction model	Error! Bookmark not defined.
Figure 6.1.2 Grid convergence for wave calibration with T=10s and H=4,538m in a water depth D=70m.....	19
Figure 6.2.2 Grid Convergency for wave induced lifting force (F_z)	20
Figure 6.2.4 Grid Convergency for wave induced drag force (F_x)	Error! Bookmark not defined.
Figure 7.1.1 Vertical soil displacement U_z (m) after the completion of the consolidation process. Wave height 4.54 m, skirt length 30 cm.....	Error! Bookmark not defined.
Figure 7.1.1 Vertical effective stress σ_z (Pa) after the completion of the consolidation process. Wave height 4.54 m, skirt length 30 cm.....	24
Figure 7.1.2 Pore pressure p (Pa) after the completion of the consolidation process. Wave height 4.54 m, skirt length 30 cm	Error! Bookmark not defined.
Figure 7.2.1 Location of cross sections through the seabed	25
Figure 7.3.1 Shear stress σ_{xz} distribution in the seabed at the t=140 s, H=16 m, skirt length 30 cm	26
Figure 7.3.2 Pore pressure distribution in the seabed at the t=140 s, H=16 m, skirt length 30 cm	Error! Bookmark not defined.
Figure 7.3.3 Vertical distributions of displacement amplitude U_{zmax} in various locations at different skirt lengths. H=4.54 m.....	28
Figure 7.3.4 Vertical distributions of pore pressure amplitude p_{max} in various locations at different skirt lengths.....	30
Figure 7.3.5 Vertical distributions of pressure gradient amplitude PG in various locations at different skirt lengths	Error! Bookmark not defined.
Figure 7.4.1 Vertical distributions of pore pressure amplitude p_{max} in various locations at different wave heights. Skirt length 10 cm.....	33
Figure 7.4.2 Vertical distributions of vertical displacement amplitude U_{zmax} in various locations at different wave heights. Skirt length 10 cm	35
Figure 7.4.3 Vertical distributions of pressure gradient amplitude PG in various locations at different wave heights. Skirt length 10 cm.....	36
Figure 7.4.4 Wave induced Lifting force (F_z) depending on the wave heights	37
Figure 7.4.5 Wave induced Drag force (F_x) depending on the wave heights	37
Figure 7.4.6 The delay between Lifting (F_z) and Drag (F_x) forces amplitudes in one wave length	38
Figure 7.5.1 Liquefaction at the 30 cm skirt length when the wave crest passes the construction	40

Figure 7.5.2 Liquefaction at the 10 cm skirt length when the wave crest passes the construction 40

List of tables

Table 2.5.1 Wave height in dependence of KC number	13
Table 5.2.1 Parameter settings for wave-structure-seabed interaction modeling in the present study	17
Table 6.1.1 Grid convergence for wave calibration with $T=10s$ and $H=4,538m$ in a water depth $D=70m$	18
Table 6.2.1 Grid Convergence for Fz	19
Table 6.2.3 Grid Convergency for wave induced drag force (FX)	21
Table 6.3.1 Grid Convergence study for Seabed Pore Pressure (results for the location at 1 m depth underneath the structure bottom center)	22
Table 6.3.2 Grid Convergence study for Seabed Pore Pressure (results for the location at 1 m depth underneath the structure bottom center)	22

1. Introduction

The interaction between waves, structure, and soil is crucial for preventing future offshore structure failures caused by geotechnical issues. Liquefaction in geotechnics refers to the state of soil where the effective stresses between individual soil grains disappear, causing the water-sediment mixture to behave like a liquid. The onset of liquefaction occurs when the water-pore pressure, in excess of the static pore-water pressure, reaches a critical value due to the introduction of waves. Due to the complexity of external dynamic wave loadings and the seabed material itself, accurately assessing wave-induced soil pore pressure and soil displacements has been a challenging task for a past two decades. Failure to address this issue can result in significant damage to offshore structures. The investigation of momentary liquefaction in the seabed has been an ongoing area of research for decades, with numerous studies contributing to our understanding of this phenomenon. Since the early 1900s, researchers have been interested in studying momentary liquefaction in the seabed. The term was initially introduced by Terzaghi in his 1943 book "Theoretical Soil Mechanics," where he defined it as a state in which the pore pressure of soil increases to a level that results in a reduction of effective stress to zero.

Since the 1970s, various investigations have been conducted on the response of soil induced by waves. These investigations have included analytical approximations by Putnam (1949), Yamamoto et al. (1978), Mei and Foda (1981), Okusa (1985), Jeng and Hsu (1996), Sumer and Fredsøe (2002), Jeng and Seymour (2007); numerical modeling by Thomas (1989, 1995), Jeng and Lin (1996), Madga (1996, 2000), Mostafa et al. (1999), Jeng (2003a), and Dunn et al. (2006); and physical modeling by Tsui and Helfrish (1983), Zen and Yamazaki (1990), Sassa and Sekiguchi (1999), Sumer et al. (2006, 2007). Jeng (2012) has reviewed the contributions and limitations of most of these works. In 2016 Elsafti and Oumeraci created WSSI solver named geotechFoam, which was able to perform two-dimensional elastic seabed simulations including wave influence on the seabed. Li et al. (2018) has integrated Tang et. al. (2014) anisotropic poro-elastic solver to the three-dimensional FVM-based model for medium and coarse sand soil. More recent studies have focused on new techniques for measuring soil liquefaction, such as using fiber optic sensors (Le et al., 2021) and X-ray computed tomography (Kawakami et al., 2021). These advancements have provided new insights into the behavior of soil during momentary liquefaction and can aid in developing more accurate models for predicting and preventing offshore structure failures.

This study is centered on exploring the occurrence of momentary liquefaction in the poro-elastic seabed and incorporates Biot's u-p approximation model in a FVM-based framework with anisotropic considerations. For free surface wave generation, absorption and modeling the interaction between waves and structure, the we solver wave2Foam (Jacobsen et.al., 2012) is applied. To solve the soil consolidation process under static force the biotConsolidationFoam solver based on quasi-static Biot's model was used. A finite volume (FV) soil solver, named anisoUpFoam, is utilized in conjunction with FV wave solver and soil solver to investigate the interaction between waves and the seabed-soil-structure system (WSSI).

This study is divided to three 2D cases which were implemented using toolbox developed by Li et.al. (2022). All three cases distinguished by various wave height and KC number. Okusa liquefaction criteria is applied.

2. Theoretical background

2.1. Skirted GRP covers

Skirted GRP covers are protective covers that are used to protect subsea pipelines in offshore installations. They are made of Glass Reinforced Plastic (GRP), which is a durable and corrosion-resistant material. The covers have a low profile design, and are installed around the pipelines on the seabed using suction anchors or steel piles.



Figure 2.1.1 Skirted GRP Cover

The skirted design of the covers extends downwards from the top cover to create a barrier around the pipeline, which helps to prevent debris and other objects from coming into contact with the pipeline. The skirt is typically made of a flexible material that can conform to the contours of the seabed and provide a tight seal around the pipeline. The use of GRP material makes the covers lightweight, easy to install, and resistant to corrosion. The low profile design reduces drag and uplift forces caused by ocean currents, while the skirted design helps to reduce scouring of the seabed around the pipeline. Skirted GRP covers are an effective solution for protecting subsea pipelines in offshore installations, and are commonly used in the oil and gas industry. They provide long-lasting protection against impact and abrasion, helping to ensure the safety and reliability of subsea pipelines. Skirted GRP covers are designed to withstand the harsh environmental conditions of offshore installations, including high waves, strong currents, and corrosive seawater. They are also resistant to UV radiation, which can cause degradation of some materials over time. The installation of skirted GRP covers is a relatively straightforward process, and can be completed using remote-operated vehicles (ROVs). The covers can be designed to fit specific pipeline sizes and configurations, and can be easily removed and replaced if necessary.

2.2 Free Surface Wave Model

To examine the interactions between waves, structures, and seabed, the incompressible Navier-Stokes equations, which include both continuity and momentum equations, are employed in the analysis of the wave domain.

$$\nabla \cdot \mathbf{u} = 0 \quad (1)$$

$$\frac{\partial \mathbf{u}}{\partial t} + (\mathbf{u} \cdot \nabla) \mathbf{u} = -\frac{1}{\rho_f} \nabla p_d + \mathbf{g} + \frac{1}{\rho_f} \nabla \cdot \boldsymbol{\tau} \quad (2)$$

The Navier-Stokes equations employ the following definitions for the variables: the velocity vector \mathbf{u} , has components in the x , y , and z directions; \mathbf{g} - gravitational acceleration; ρ_f represents the density of the fluid, which can be either air (ρ_a) or water (ρ_w); p_d denotes the dynamic wave pressure, which is given by $p_d = p_t - \rho_f \mathbf{g} \cdot \mathbf{x}$, where p_t refers to the total pressure and $\mathbf{x} = (x, y, z)$ is the Cartesian coordinate vector. The viscous stress tensor is denoted by τ_{ij} and is expressed using Einstein notation. In the case of a Newtonian fluid, these variables are utilized in the Navier-Stokes equations.

$$\tau_{ij} = 2\mu\sigma_{ij} \quad (3)$$

where μ represents the dynamic molecular viscosity, which uses μ_{air} for air and μ_{water} for water. The term σ_{ij} is defined in the following way:

$$\sigma_{ij} = \frac{1}{2} \left(\frac{\partial u_i}{\partial x_j} + \frac{\partial u_j}{\partial x_i} \right) \quad (4)$$

The Navier-Stokes equations utilize the velocity components u_i and u_j in the x , y , and z directions, where $i, j \in [1, 2, 3]$. These equations are applied to solve for two immiscible fluids concurrently, with their movements tracked using a scalar field α . This field represents a value of 0 for air, 1 for water, and any intermediate value as a mixture of the two fluids. An advection equation is employed to model the distribution of α .

$$\frac{\partial \alpha}{\partial t} + \nabla \cdot \alpha \mathbf{u} + \nabla \cdot [\alpha(1 - \alpha) \mathbf{u}_r] = 0 \quad (5)$$

The compression term on the left-hand side prevents the interface from being overly spread out, and the relative velocity \mathbf{u}_r is also present. By utilizing α , it is possible to describe variations in fluid properties throughout space, using a weighting approach.

$$\Phi = \alpha \Phi_{water} + (1 - \alpha) \Phi_{air} \quad (6)$$

where Φ is a fluid property, such as ρ_f and μ .

2.3 Isotropic Poro-Elastic Soil Model

The present study utilizes the classical Biot's consolidation equations (Biot, 1941) to simulate the behavior of soil, which considers the interaction between the solid skeleton and pore fluids and the isotropic properties of the soil. It is assumed that the seabed is fully saturated, and the soil skeleton follows Hooke's law with elastic properties.

Constitutive relations

In this research, the convention followed in computational continuum mechanics is applied, where the tension stress is considered positive, and compression stress is taken as negative. The total stress for the saturated porous medium is defined as follows:

$$\sigma = \sigma' - pI \quad (7)$$

The effective stress tensor of the soil skeleton is denoted by σ' , while σ represents the total stress tensor of the soil mixture. The pore fluid pressure is represented by p , and stands for the identity tensor. The effective stress-strain relation is expressed using the generalized Hooke's law.

$$\sigma' = C : \varepsilon \quad (8)$$

The relationship between strain and displacement is represented by the following expression:

$$\varepsilon = \frac{1}{2}(\nabla U + (\nabla U)^T) \quad (9)$$

where ε is the strain tensor, U is the soil skeleton displacement vector.

Quasi-static model for consolidation analysis

In the present research, the Biot's model is utilized to analyze the behavior of soil, which is regulated by two governing partial differential equations: one vector equation for momentum equilibrium and one scalar equation for mass conservation. As the consolidation analysis involves the application of a static gravitational force to the seabed, the Biot's model is used in its quasi-static form due to the low frequency of the process. The soil domain in the consolidation analysis is controlled by a quasi-static momentum balance equation for the soil mixture and a mass balance equation for the pore fluid, which is based on Darcy's law. The quasi-static momentum balance equation is presented below:

$$\nabla * [C : \frac{1}{2}(\nabla U + (\nabla U)^T)] - \nabla p + \rho g = 0 \quad (10)$$

Where C is fourth-order elastic stiffness tensor, U is the soil displacement, p is the excess pore fluid pressure, g is the gravitational acceleration. The saturated density of the soil mixture is represented by ρ in the given context.

$$\rho = n\rho_f + (1 - n)\rho_s \quad (11)$$

Darcy's law-based mass balance equation of the pore fluid is given as a function of n , the porosity, ρ_s , the soil density, and ρ_f , the water/fluid density. The equation is formulated as follows:

$$\frac{n}{K'} \frac{\partial p}{\partial t} - \frac{1}{\gamma_w} \nabla * (k * \nabla p) + \frac{\partial}{\partial t} (\nabla * U) + \frac{k}{g} (\nabla * g) = 0 \quad (12)$$

The equation includes the values of n , representing the soil porosity, γ_w , representing the specific weight of water in soil, and k , representing the diagonal permeability tensor with values of k_x , k_y , and k_z . The computation of the bulk modulus of the compressible pore flow K' involves the use of the formulation provided by Vafai and Tien (1981).

$$\frac{1}{K'} = \frac{1}{K_w} + \frac{1 - S_r}{p_a} \quad (13)$$

where S_r is the degree of soil saturation, K_w is the bulk modulus of pure water and $p_a = p_f g h_w$ is the sum of the atmospheric pressure and the static water pressure at the seabed.

u-p approximation model for wave-induced and structure-induced seabed response

The u-p approximation model, which offers superior accuracy for oscillating problems compared to the quasi-static form and better efficiency for most engineering problems compared to the fully-dynamic form, is used in this work to model wave-induced seabed response. The analysis commences after the installation of the gravity structure and completion of the consolidation process, at which point the seabed soil has established equilibrium with the structure's weight. The governing equations for the u-p approximation model are used to analyze the wave effect on the soil.

$$\nabla * [C: \frac{1}{2} (\nabla U + (\nabla U)^T)] - \nabla p - \rho \frac{\partial^2 U}{\partial t^2} = 0 \quad (14)$$

$$\frac{n}{K'} \frac{\partial p}{\partial t} - \frac{1}{\gamma_w} \nabla * (k * \nabla p) + \frac{1}{g} \nabla \left(k * \frac{\partial^2 U}{\partial t^2} \right) + \frac{\partial}{\partial t} (\nabla * U) = 0 \quad (15)$$

The force balance equation, Eqn. 14, does not include the gravitational term ρg . This is because the pure wave-induced soil response analysis adopts the partial dynamic u-p approximation form, which assumes an equivalent status between the structure and the soil at the start of the analysis. Therefore, the only external force considered in Eqn. 14 is the dynamic wave pressure, represented by the term.

2.4 Finite volume method based approach

The WSSI analysis is a numerical simulation technique used to predict the seabed response due to the propagation of ocean waves. The Finite Volume Method (FVM) is a widely used approach for solving such problems and can be used to solve the WSSI equation.

The FVM is a numerical technique used to solve partial differential equations (PDEs) by discretizing the domain into a finite number of control volumes. In the case of WSSI analysis, the seabed domain is divided into a mesh of control volumes, and the PDE describing wave propagation and seabed soil response is solved for each control volume.

The FVM approach for WSSI analysis involves the following steps:

1. Discretization of the seabed domain into a mesh of control volumes.
2. Definition of boundary conditions for each control volume.
3. Application of the conservation law for wave energy and momentum to each control volume.
4. Solution of the resulting linear system of equations for the unknown wave and seabed response variables.
5. Calculation of the wave-induced seabed soil response, including the pore pressure, effective stress, and soil deformation.

The FVM approach has several advantages for WSSI analysis, including its ability to handle complex geometries, the ability to handle non-linear wave propagation and seabed soil response, and its accuracy for capturing the details of the seabed soil response. However, the FVM approach can also be computationally intensive, and requires significant computational resources to solve problems with large domains and complex geometries.

In this study mass balance and momentum equations are divided into two parts: the implicit and explicit discretization. The explicit part includes the coupling effect from other variables and is evaluated based on the previous iteration or the initial condition.

The inter-component coupling described in Equation (16) can be separated into two components, namely implicit and explicit.

$$\sigma' = C : \varepsilon = \underbrace{K * \nabla U}_{\text{implicit}} + \underbrace{C : \varepsilon - K * \nabla U}_{\text{explicit}} \quad (16)$$

The K represents a diagonal stiffness tensor of size 3 x 3, defined by

$$K = \begin{bmatrix} A_{11} & 0 & 0 \\ 0 & A_{22} & 0 \\ 0 & 0 & A_{33} \end{bmatrix} \quad (17)$$

By rearranging Equation (10) and Equation (12), they can be expressed in the implicit-explicit format for the Finite Volume Method (FVM)

$$\underbrace{\nabla(K * \nabla U)}_{\text{implicit}} = \nabla * \underbrace{\left[C: \frac{1}{2} (\nabla U + (\nabla U)^T) + \nabla(K * \nabla U) - \nabla p + \rho g \right]}_{\text{explicit}} \quad (18)$$

$$\underbrace{\frac{n}{K'} \frac{\partial p}{\partial t} - \frac{1}{\gamma_w} \nabla * (k * \nabla p)}_{\text{implicit}} = \underbrace{-\frac{\partial}{\partial t} (\nabla * U) - \frac{k}{g} (\nabla * g)}_{\text{explicit}} \quad (19)$$

The implicit-explicit format for the Finite Volume Method (FVM) can also be used for the u-p approximation model in wave effect analysis, and can be expressed as:

$$\underbrace{\nabla(K * \nabla U)}_{\text{implicit}} = \nabla * \underbrace{\left[C: \frac{1}{2} (\nabla U + (\nabla U)^T) + \nabla(K * \nabla U) - \nabla p - \rho \frac{\partial^2 U}{\partial t^2} \right]}_{\text{explicit}} \quad (20)$$

$$\underbrace{\frac{n}{K'} \frac{\partial p}{\partial t} - \frac{1}{\gamma_w} \nabla * (k * \nabla p)}_{\text{implicit}} = \underbrace{-\frac{\partial}{\partial t} (\nabla * U) - \frac{\nabla}{g} \left(k * \frac{\partial^2 U}{\partial t^2} \right)}_{\text{explicit}} \quad (21)$$

2.5 Keulegan-Carpenter Number

To avoid turbulence modeling the KC number for all cases is relatively small and less than 5.

Table 2.5.1 Wave height in dependence of KC number

KC number	Wave amplitude velocity (m/s)	Wave height (m)
0.35	0.07	1.94
0.58	0.37	3.24
0.81	0,16	4.53
1.44	0,29	8
2.89	0,59	16

The KC number equation is given below:

$$KC = \frac{u_a * T}{D} \quad (22)$$

3. BOUNDARY COUPLING ALGORITHM

where T is the wave period, D is the diameter of the structure and u_a is wave velocity amplitude, which can be described by using linear wave theory equation for intermediate water depth ($1/20 < d/L < 1/2$).

$$u_a = \frac{\varepsilon_0 k g \cosh k(z+d)}{\omega \cosh(kd)} \sin(\omega t - kx) \quad (23)$$

where wave length denoted by L , wave amplitude denoted by ε_0 , $\omega = 2\pi/T$, $k = 2\pi/L$, d is water depth, z is vertical co-ordinate, positive upward, origin at SWL. For linear wave theory it can be assumed that $z = 0$.

3 Boundary Coupling Algorithm

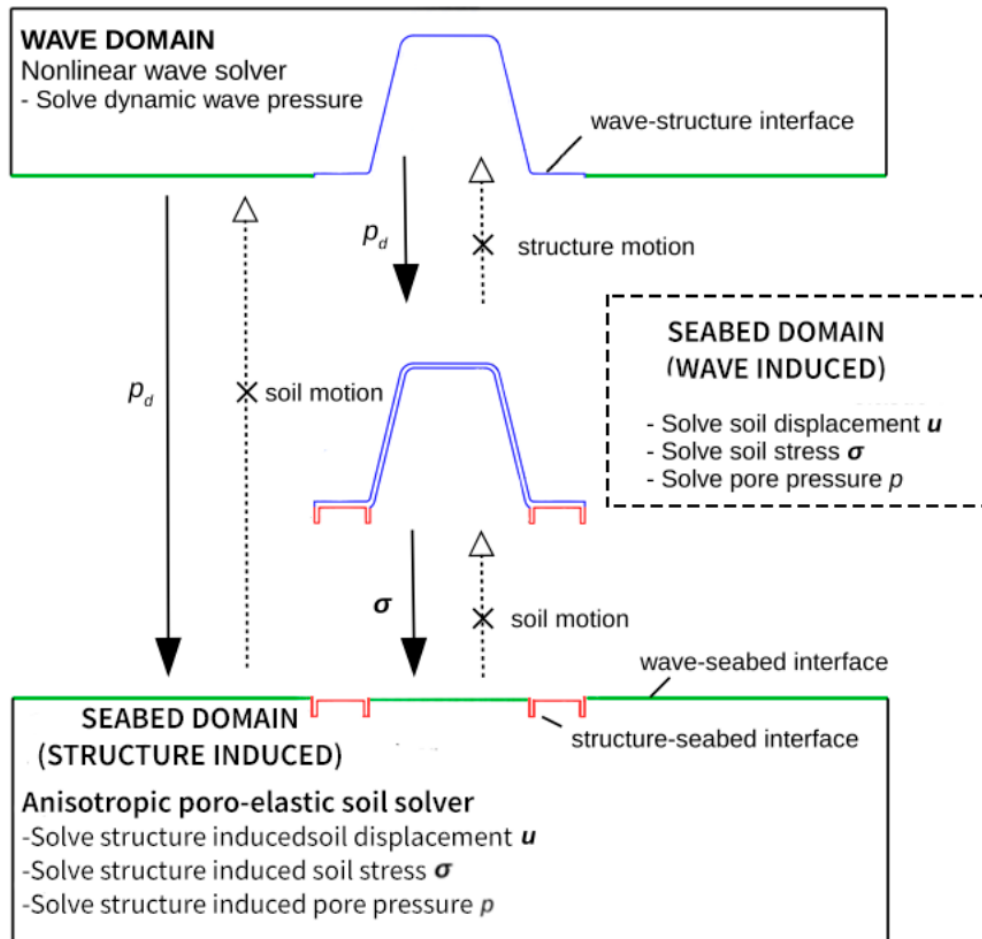


Figure 3.1 Boundary coupling algorithm of wave-structure-seabed interaction

The coupling process involves the exchange of dynamic wave pressure and structure-induced seabed stress between the waves and seabed domains. To ensure computational efficiency, a one-way coupling algorithm is adopted, with data transferred only in the direction from the

waves to the seabed. This approach enables the use of different grid sizes and time steps in the three or four domains, improving computational efficiency and reducing power requirements.

4 Model Validation

To validate the FV u-p approximation soil solver in this study an experimental data from Tsai and Lee (1995) investigating pore pressure induced by standing waves in a sand bed near a vertical wall was used. Li et al. (2018) also validated their quasi-static Biot poro-elastic solver using the same experiment. The present study replicated the experiment using the u-p approximation soil solver and compared the numerical results to both the experimental data and the numerical results obtained from the quasi-static Biot poro-elastic solver in Li et al. (2018).

5 Model Application

The present work focuses on skirted GRP cover with various skirt lengths value – 10 cm, 20 cm, 30cm. The geometry of the structure is shown in Figure 5.2. The numerical model, consisting of two physical domains – waves and seabed, which represents the sum of structure-induced soil and wave-induced soil domains data. Model is presented in an integrated layout in Figure 5.1.

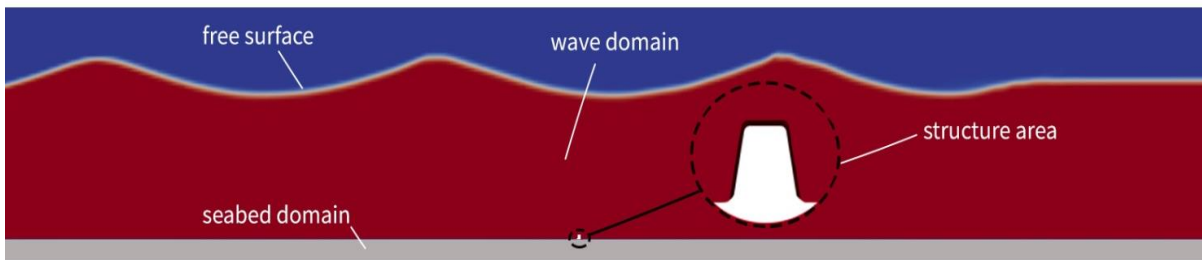


Figure 5.1 Illustration of the wave-structure-seabed interaction

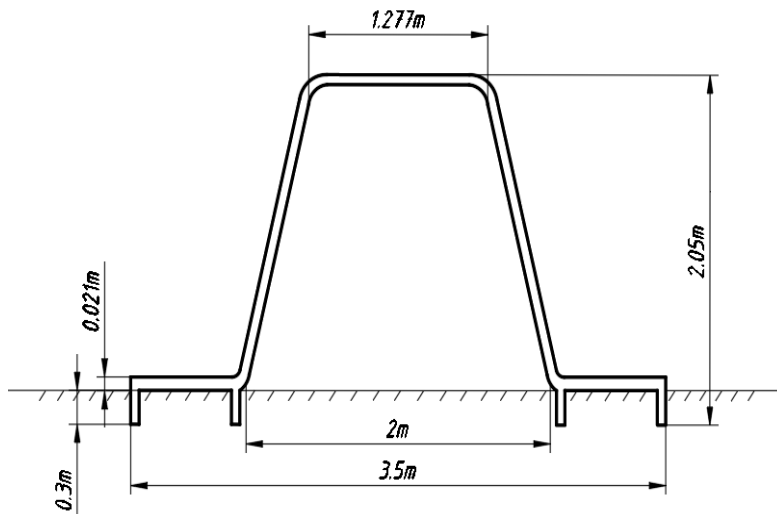


Figure 5.2 Geometry parameters of the skirted GRP cover in the 2D. Skirt length 30 cm

5.1 Wave domain settings

The Cartesian coordinate system $x; y; z$ is used to build the entire numerical system, where $z = 0$ is representing the undisturbed free surface, x is positive toward the wave propagation direction, y is positive toward the back of domain and z is positive upwards. For 2D simulation y directions sets to 1.

Table 5.1.1 shows the parameters of the waves considered in the present study., The wave period T is 10 s, and the wave height varies from 4.53 m until 16 m. All wave heights are investigated in the parametric study. To model the waves, the 2nd-order Stokes wave model based on Fenton's Stokes wave theory (Fenton, 1985) is used for 4.53 in this study and the 3rd-order Stoke wave model for 8 m and 15 m wave heights.

To prevent wave reflection from the outlet boundary, the numerical model incorporates an inlet relaxation zone of one wave length (L), a working zone of two wave lengths ($2L$), and an outlet relaxation zone of two wave lengths ($1.25L$). Jacobsen et al. (2012) provide a detailed explanation of the numerical wave tank relaxation techniques utilized in this study. Inlet velocity value is specified as the theoretical wave velocity. Outlet velocity set as a zero. At the interface with the atmosphere, the pressure is defined as equal to the atmospheric pressure (p_0), and the velocity is set to a 'zero-gradient' boundary condition.

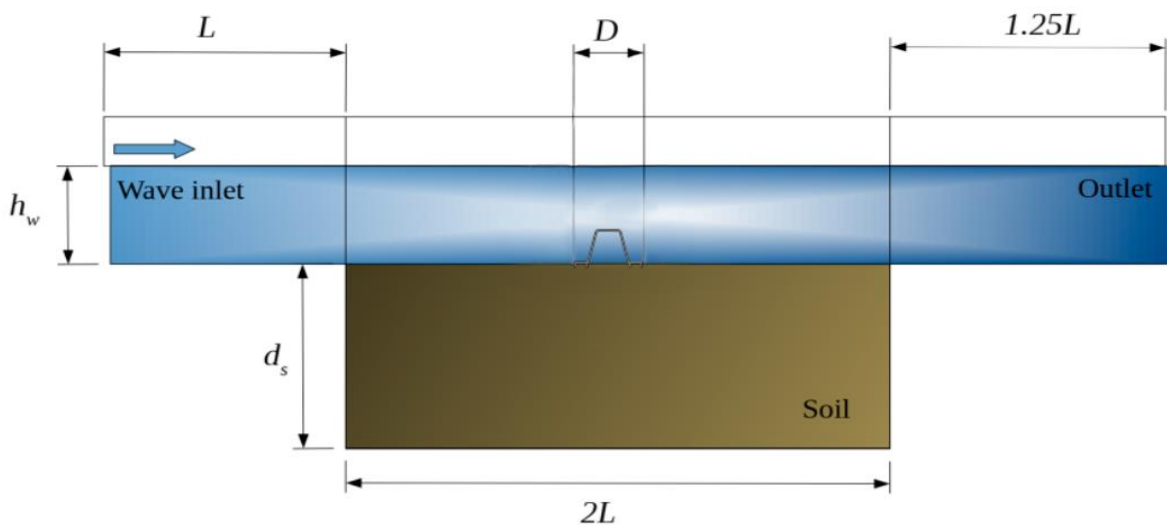


Figure 5.1.1 sketch of the numerical layout for the wave-structure-seabed interaction model

5.2 Seabed Domain Settings

The total seabed domain consists of structure-induced soil and wave-induced soil domains. Seabed parameters: Seabed thickness is 10m with domain length is 4.25L. Soil set to be isotropic with permeability equals to 0.00077 m/s, soil porosity is 0.35. More soil settings are shown in table 5.2.1.

The interface between the waves and seabed is characterized by the absence of effective soil stresses, which results in zero traction at the seabed surface. At this interface, the pore pressure is equivalent to the dynamic wave pressure acting on the seabed. Total soil displacement, total stress, total pore pressure merged from two separate soil domains data.

Wave parameters			
Water depth (m)	70	70	70
Wave period T (s)	10	10	10
Wave height H (m)	4.54	8	16
Wave type	Stokes-second	Stokes-third	Stokes-third
Subsea cover parameters			
Density (kg/m ³)	1990	1990	1990
Poisson ratio	0.29	0.29	0.29
Skirt parameters			
Skirt length (cm)	10,20,30	10,20,30	10,20,30
Density (kg/m ³)	1990	1990	1990
Seabed parameters			
Young's modules (N/m ²)	6.86×10^7	6.86×10^7	6.86×10^7
Poisson ratios	0.35	0.35	0.35
Permeability (m/s)	$k_x = k_z = 0.00077$	$k_x = k_z = 0.00077$	
Saturation degree (S_r)	0.98	0.98	0.98

Table 5.2.1 Parameter settings for wave-structure-seabed interaction modeling in the present study

6 Convergence studies

6.1 Wave Calibration

The study simulates intermediate water depth nonlinear waves and verifies them through convergence studies with four sets of simulations. The results of the convergence wave elevation study are shown in Fig. 6.1.2 and Table 6.1.1.

The mesh is refined by changing the grid resolution at the free surface and structure areas. The grid size is gradually increased for each simulation besides Mesh№4, where the domain height was significantly changed. The analysis shows that Mesh№2 and Mesh№4 have an acceptable accuracy level with a percentage difference of 5.53% and 5.22%, respectively, compared to the initial condition of wave height $H=4.538$ m. Increasing the number of grid points from Mesh№2 to Mesh№3 by 67% sufficiently reduces the difference ratio by 3.49%. Mesh№4 has been chosen for further simulations.

Table 6.1.1 Grid convergence for wave calibration with $T=10$ s and $H=4,538$ m in a water depth $D=70$ m

Mesh	Number of grids	Grids number per wave length	Wave crest amplitude	Wave through amplitude	Wave height	Percentage difference of the wave heights
Mesh №1	10893	2412	2,31	-2,05	4,36	-3,92%
Mesh №2	21517	4764	2,27	-2,08	4,28	-5,53%
Mesh №3	65436	14489	2,37	-2,07	4,44	-2,04%
Mesh №4 (domain height 100m)	22178	4917	2,28	-2,02	4,30	5,22%

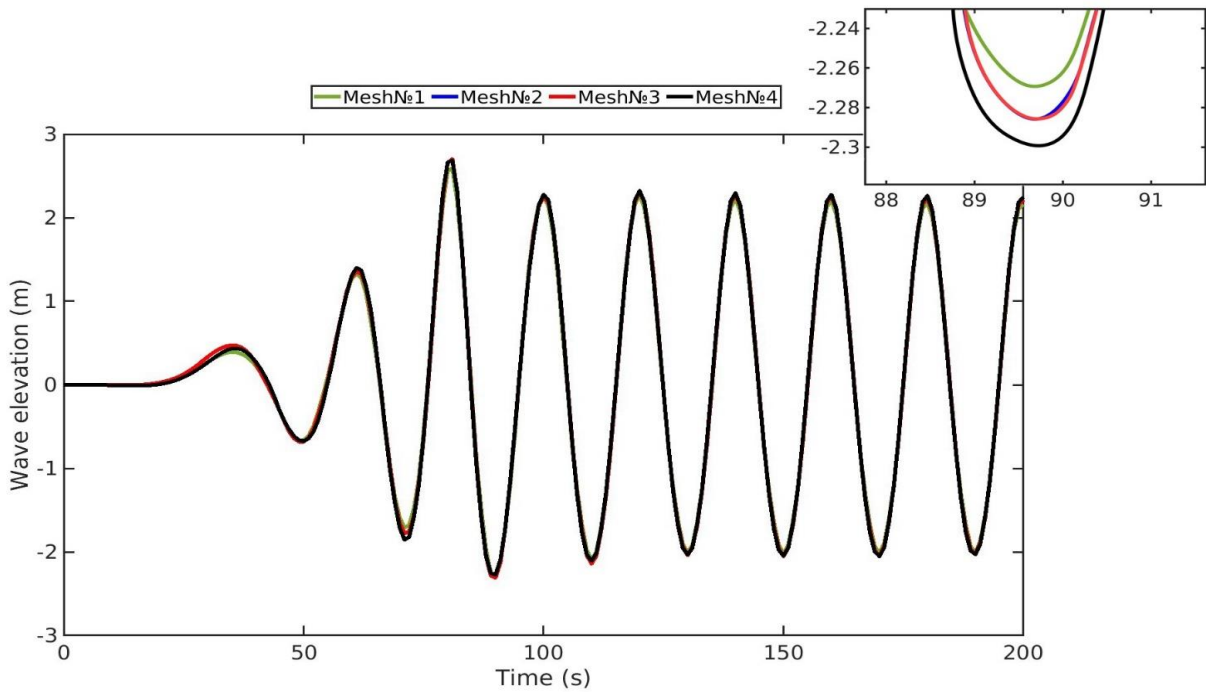


Figure 6.1.2 Grid convergence for wave calibration with $T=10s$ and $H=4,538m$ in a water depth $D=70m$

6.2 Grid Convergence for Lifting Force (F_z) and Drag Force (F_x)

A 2D grid convergence study for F_z and F_x for skirted GRP cover is implemented with the same 4 sets of wave domains as they are in wave convergence study. Results are compared at the structure center location ($x=0$) and provided in the Table 6.2.1, Figure 6.2.2 for F_z and Table 6.2.3, Figure 6.2.4 for F_x respectively.

Table 6.2.1 Grid Convergence for F_z

Mesh	Number of grids	Grids number per wave length	Maximum force (kN/m)	Minimum force (kN/m)	Relative change
Mesh №1	10893	2412	9	-9,7	3%
Mesh №2	21517	4764	9,1	-9,7	3%
Mesh №3	65436	14489	9	-9,9	1%
Mesh №4 (domain height - 100m)	22178	4917	9,2	-10	

The force that acts upward on a structure due to the dynamic pressure of a wave is known as the wave lifting force.

$$f_L = \frac{1}{2} \rho C_L D u |u| \quad (24)$$

Where C_L -lift coefficient, ρ is the density of the water, D is the diameter of the structure and u is the horizontal water particle velocity.

Figure 6.2.2 shows that Mesh№4 and Mesh№3 present close results although the 3rd mesh number of grids is sufficiently higher. Relative change between all of the meshes presented in the Table 6.2.1. The mesh №4 is chosen to be used in the next study stages.

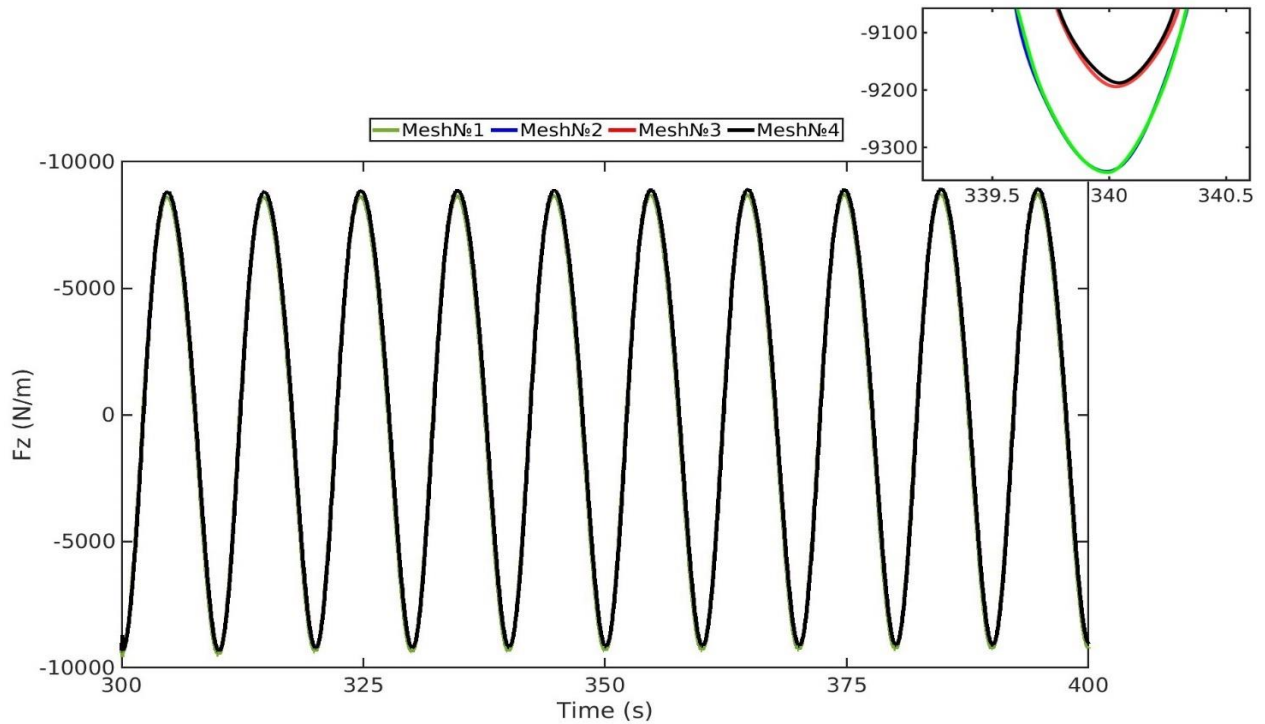


Figure 6.2.2 Grid Convergency for wave induced Lifting force (F_z)

When a wave passes a structure, the interaction between the water and the structure generates a frictional force called the drag force. This force is acting on the structure in the direction of the wave's motion.

$$f_D = \frac{1}{2} \rho C_D D u |u| \quad (25)$$

Where ρ is the density of the water, C_D is the drag coefficient, D is the diameter of the structure and u is the horizontal water particle velocity. The grid convergence study for wave induced drag force (F_X) is shown in Table 6.2.3. The relative change between the Mesh№4 and Mesh№3 is only 1%. The mesh№4 is chosen for the following study analysis.

Table 6.2.3 Grid Convergency for wave induced drag force (F_X)

Mesh	Number of grids	Grids number per wave length	Maximum force (kN/m)	Minimum force (kN/m)	Relative change
Mesh №1	10893	2412	1,53	-1,25	3%
Mesh №2	21517	4764	1,53	-1,26	5%
Mesh №3	65436	14489	1,53	-1,24	1%
Mesh №4 (domain height - 100m)	22178	4917	1,5	-1,24	

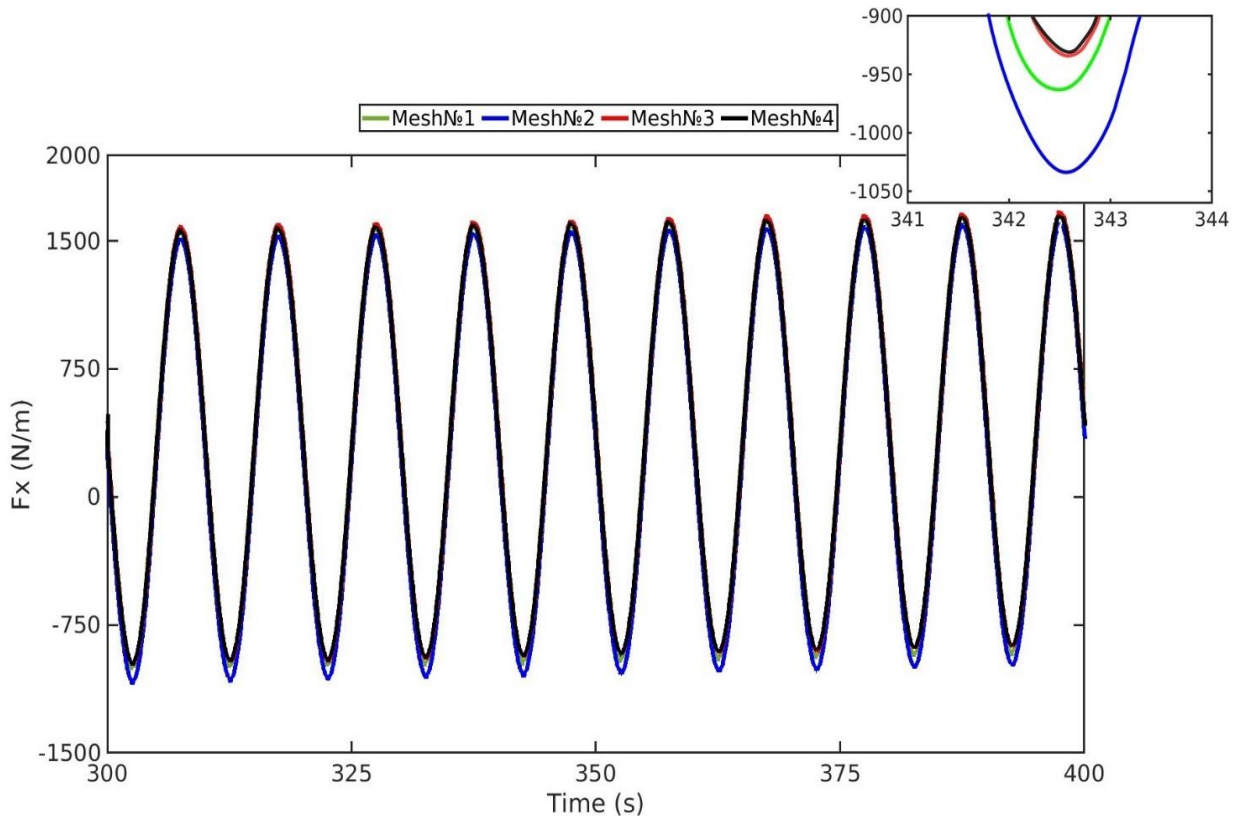


Figure 6.2.4 Grid Convergency for wave induced drag force (F_X)

6.3 Grid Convergence study for Seabed Pore Pressure

Three sets of soil meshes with various refinements of grid resolution at the structure skirts area are set to conduct seabed pore pressure grid convergence study. 1 m and 5 m depth underneath the structure bottom center are taken to extract data for figure 6.3.2. The relative change for all number of meshes is insufficient. Mesh№1 is used in the present numerical analysis.

Table 6.3.1 Grid Convergence study for Seabed Pore Pressure (results for the location at 1 m depth underneath the structure bottom center)

Mesh №	Number of grids	Maximum pressure (kPa)	Lowest pressure (kPa)	Relative change
Mesh №1 (d=1m)	61800	1,81	-1,25	
Mesh №2 (d=1m)	52226	1,8	-1,24	0,55%
Mesh №3 (d=1m)	45346	1,8	-1,24	0,55%

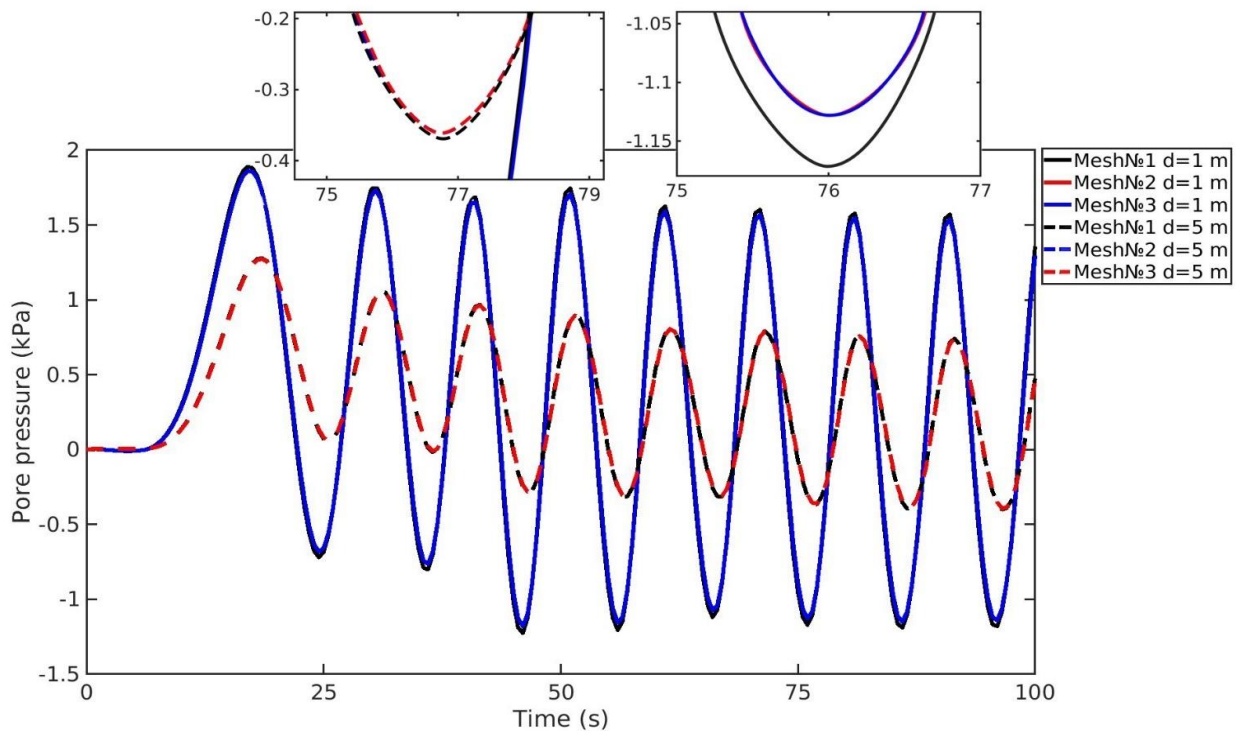


Table 6.3.2 Grid Convergence study for Seabed Pore Pressure (results for the location at 1 m depth underneath the structure bottom cen

7 Results and discussion

7.1 Consolidation

Significant amplification of effective stress within the adjacent soil conditioned by the structure and inside structure water weights exposed on the soil. The excess soil pore pressure is dissipated underneath the structure bottom center. It is important to implement the consolidation analysis first due to the possible further liquefaction risk.

As it is shown in Fig. 7.1.1, the consolidation process causes vertical soil displacement U_z with negative values reflecting to soil compression and downward movement of the soil skeleton. After the consolidation process, Fig. 7.1.2 shows the vertical effective stresses σ_z distribution in the soil. In this figure, negative σ_z values have been taken as a soil compression, while tension implies as positive.

Structure weight itself and water weight inside the structure has been taken into account while pore pressure seabed model has been developed as it is shown in Fig. 7.1.3.

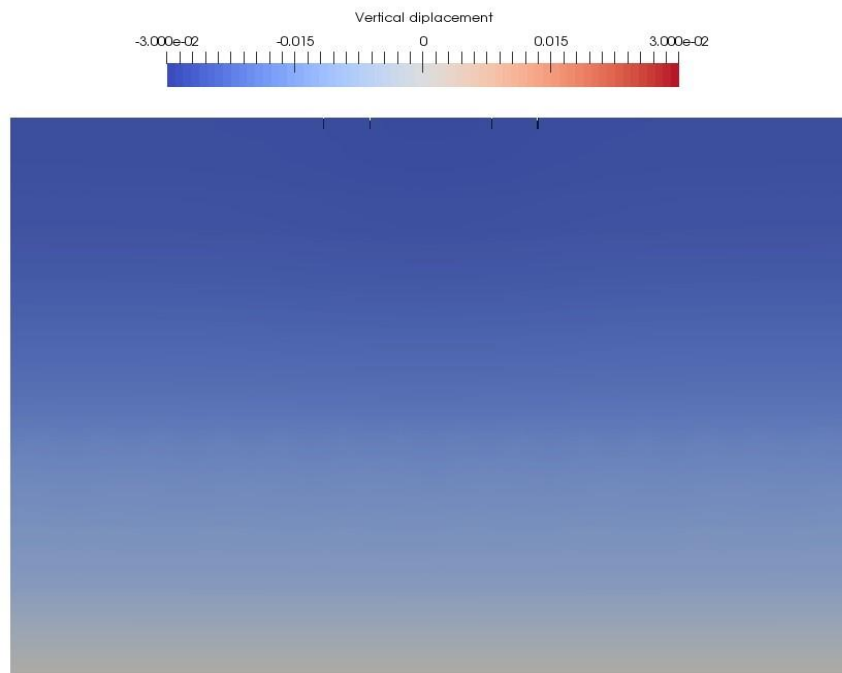


Figure 7.1.1 Vertical soil displacement U_z (m) after the completion of the consolidation process. Wave height 4.54 m, skirt length 30

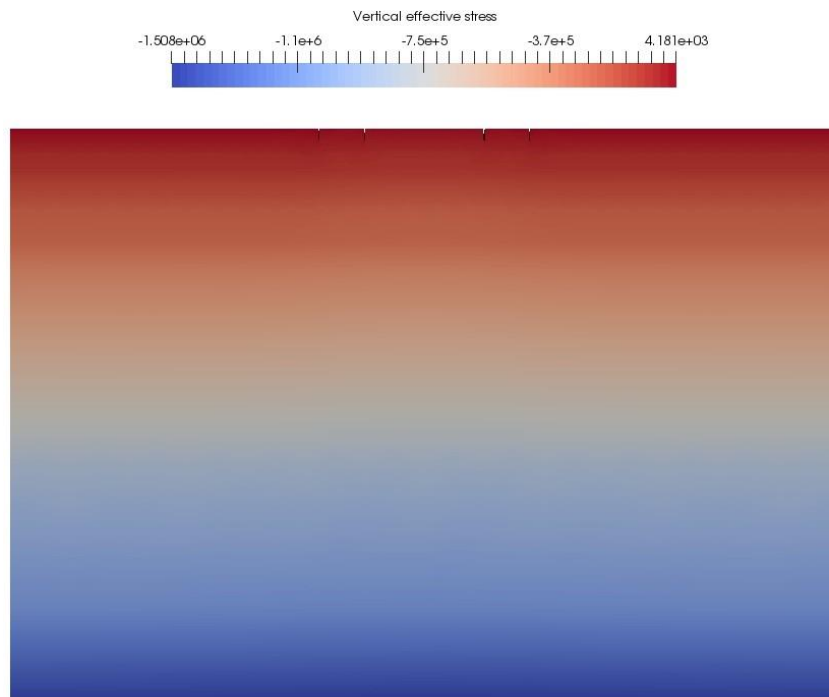


Figure 7.1.1 Vertical effective stress σ_z (Pa) after the completion of the consolidation process. Wave height 4.54 m, skirt length 30 cm

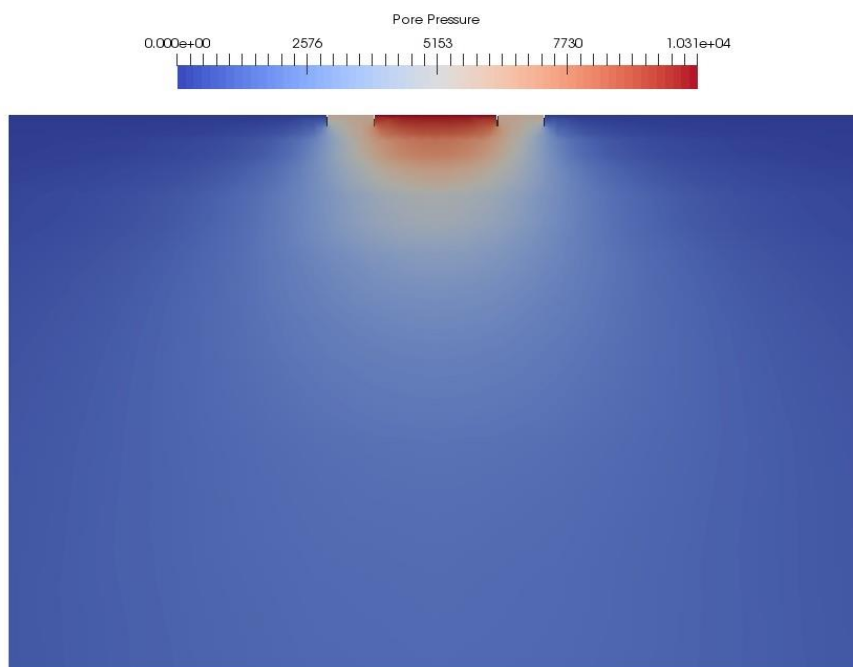


Figure 7.1.2 Pore pressure p (Pa) after the completion of the consolidation process. Wave height 4.54 m, skirt length 30 cm

7.2 Wave and Structure-Induced Seabed Responses

Further study is going to be focused on the observation, interpretation and comparison of data extracted from the cross sections locations represented in Figure 3.3.1. The flow hits the upstream skirt at the location L3 first. Location L2 reflects the processes underneath the internal upstream skirtface. As the flow passes the structure bottom center location L5, it reaches downstream location L2 and L4 which are a mirrored L1 and L3 locations. Parameters amplitude such as pore pressure, displacement, stress at the downstream side of the structure is slightly lower than at the upstream side.

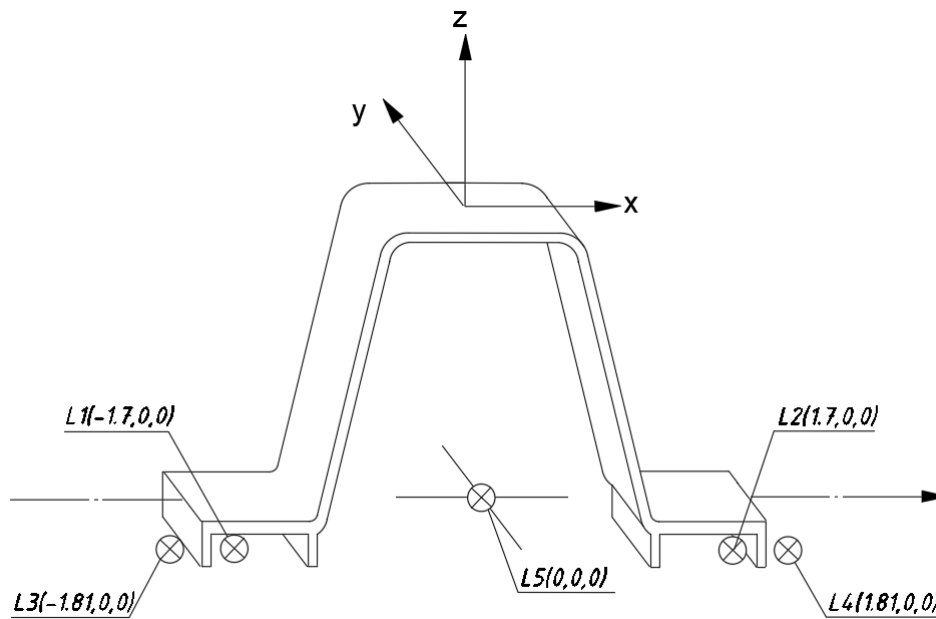


Figure 7.2.1 Location of cross sections through the seabed

Seabed response

The total shear stress is presented in Fig. 7.3.1 for the seabed soil. It can be observed that the highest value of σ_{xz} occurs right at the external downstream skirtface when the wave crest passes the construction. There are also high concentrated shearing zones at every “positive direction” skirtface. Positive direction coincides the flow direction. The lowest value of σ_{xz} occurs right at the external upstream skirtface at the same time. Nevertheless, there is only insufficient shearing effect that noticeable right underneath the structure bottom. These factors indicate that the presence of the skirts significantly amplifies the wave-induced shearing effect on the underlying seabed, and thus affects the soil responses. Seabed zone with high amplitude shear stress is prone to local plastic failure. Fig. 7.3.2 shows the total pore pressure and seepage flow in the seabed when the wave crest passes the upstream side of the construction at $t=140s$, with $H=4.53$ m. Significant upward and downward seepage flows are noticeable at the skirts area, and if these forces exceed the initial vertical effective stress, it can cause momentary soil liquefaction, posing a potential risk to the structure's safety

7.3 Parametric study

This section explores how the lifting force (F_z), drag force (F_x), total vertical soil displacement of, distribution of total pore pressure, total pressure gradient and likelihood of liquefaction at the skirfaces change under varying dynamic wave pressure amplitudes produced by a range of simulated wave heights. The study considers several wave heights of 4.54 m, 8 m, and 16 m with a wave period of 10 s. The isotropic poro-elastic soil model utilized in this study primarily focuses on assessing the risk of momentary liquefaction around the structure.

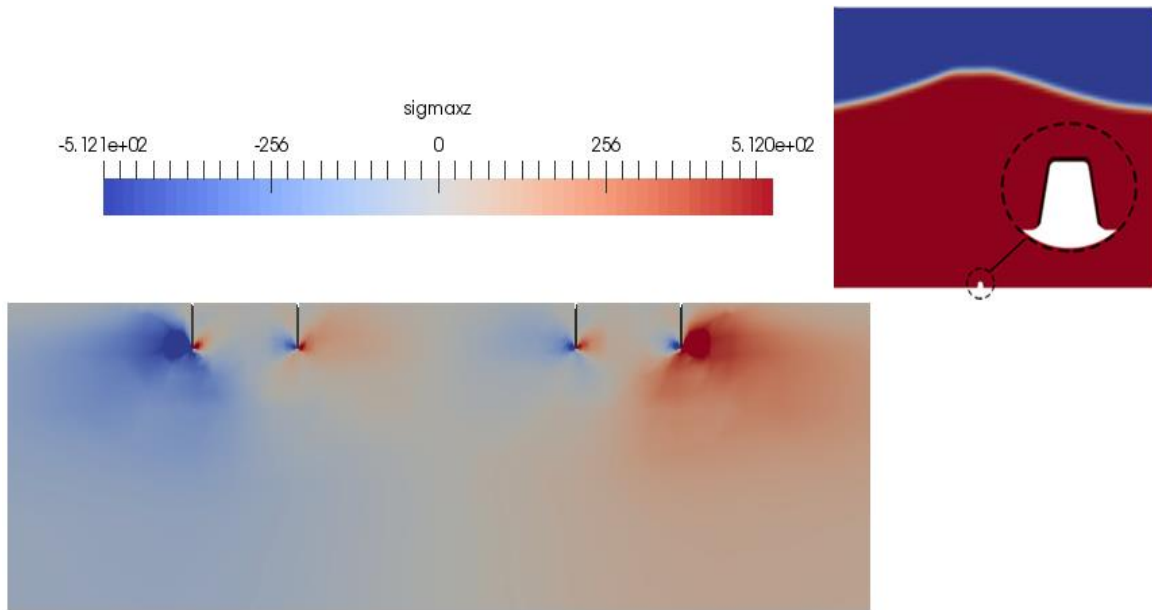


Figure 7.3.1 Shear stress σ_{xz} distribution in the seabed at the $t=140$ s, $H=16$ m, skirt length 30 cm

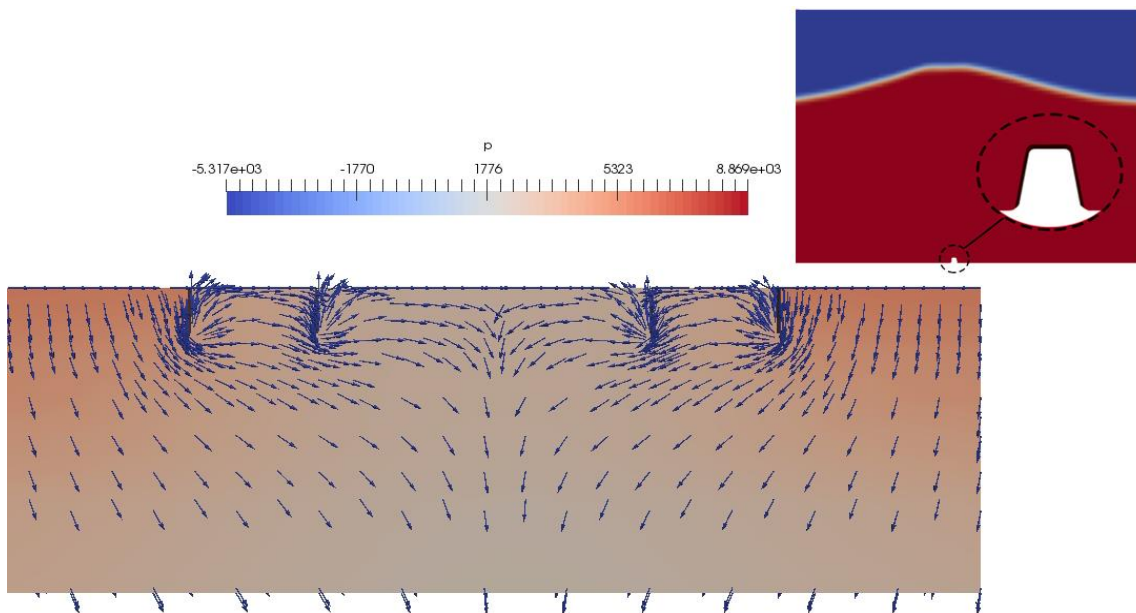
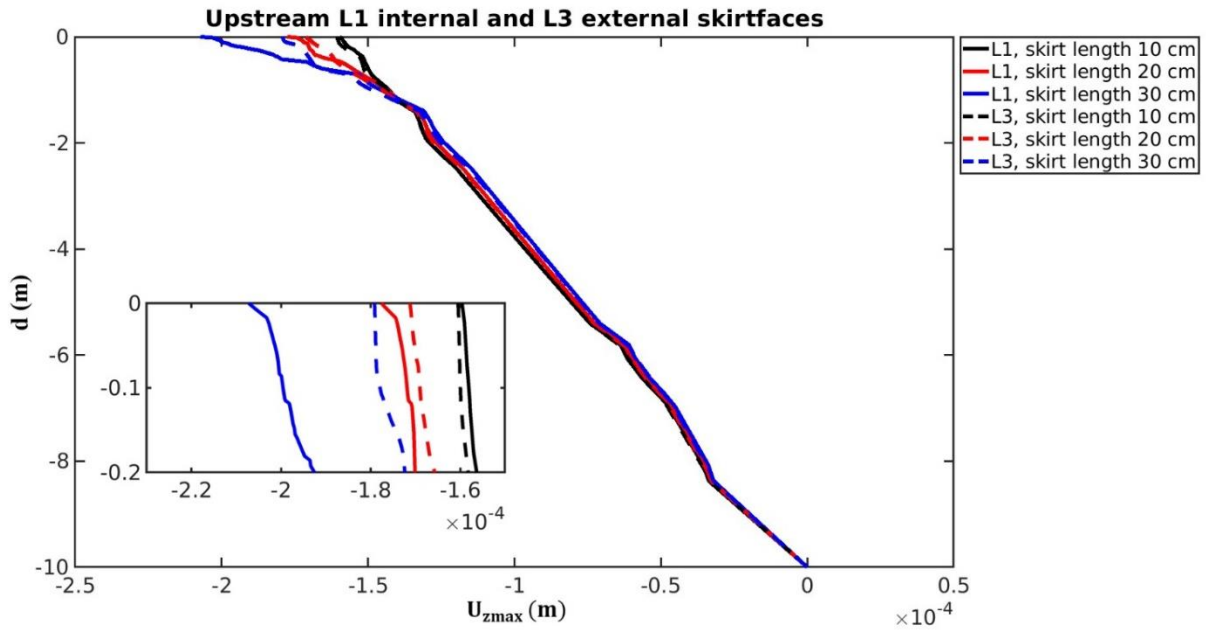


Figure 7.3.2 Pore pressure distribution in the seabed at the $t=140$ s, $H=16$ m,
skirt length 30 cm

Soil Displacement

The change of dynamic wave pressure imposed on the flat horizontal seabed surface is found to affect the vertical soil displacement. Fig. 3.4.1. examines the locations at the upstream side L3 (-1.81, 0, 0), L1 (-1.7, 0, 0), at the downstream side L4 (1.81, 0, 0), L2 (1.7, 0, 0) and the structure bottom center L5 (0, 0, 0). The maximum vertical soil displacement U_{Zmax} within a wave cycle at different skirt lengths is illustrated in Fig. 7.3.3. The results demonstrate that the vertical soil displacements at the skirts area are greater than at the structure bottom center. Additionally, it is observed that internal skirtface areas locations L1 and L3 have larger amplitude than external skirtface areas locations L2 and L5. Comparisons provided in the figures below.



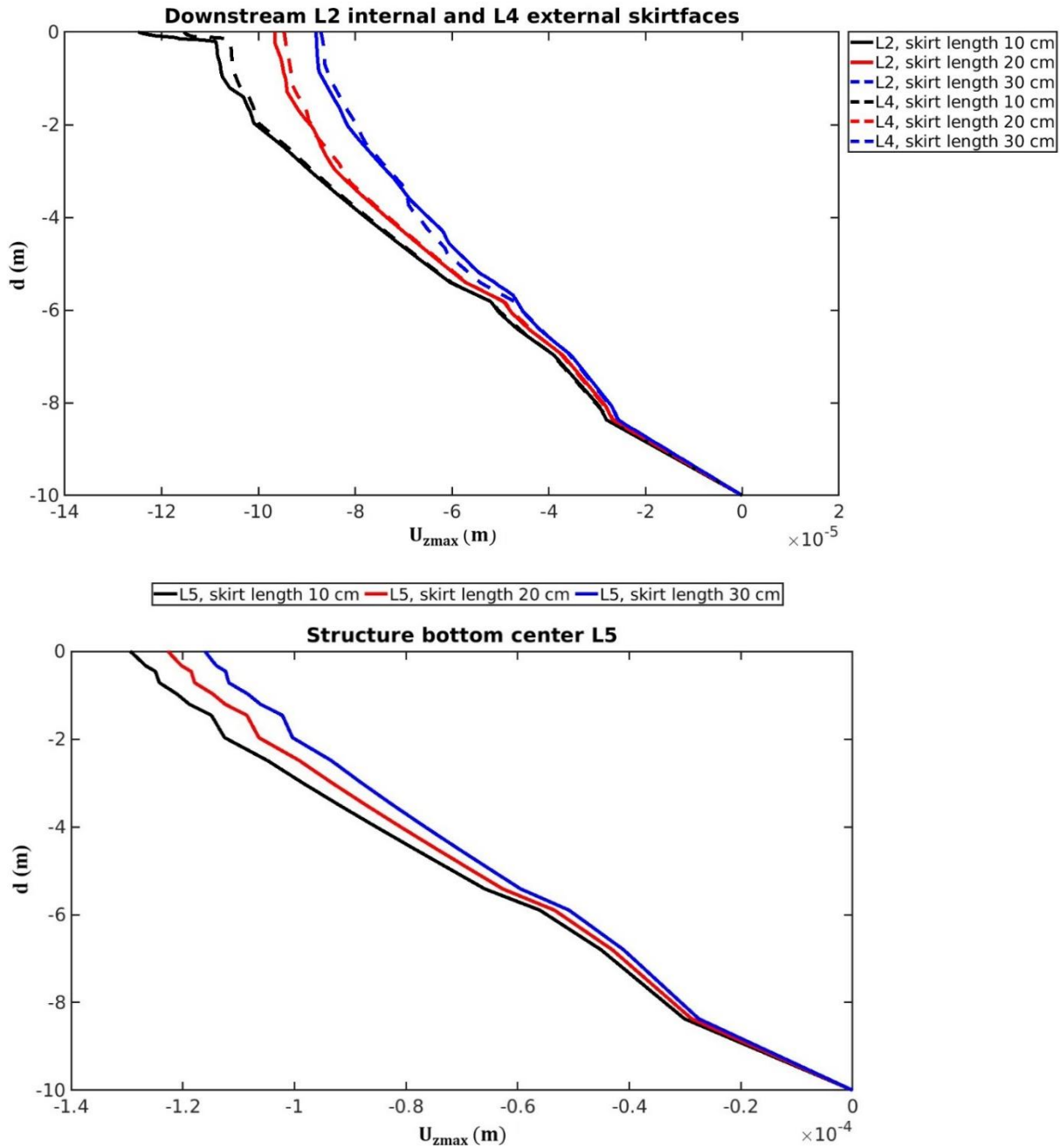
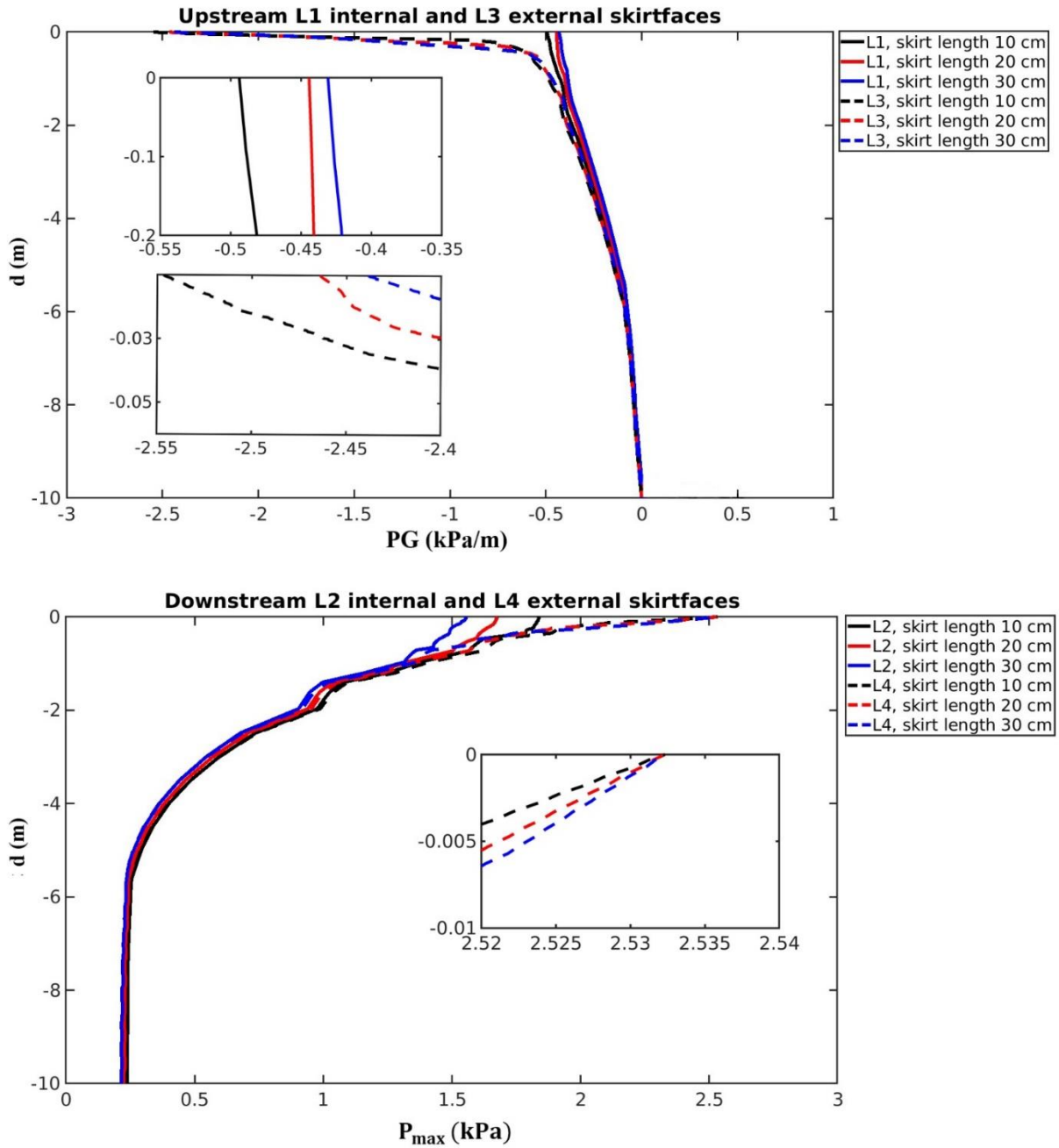


Figure 7.3.3 Vertical distributions of displacement amplitude U_{zmax} in various locations at different skirt lengths. $H=4.54$ m

Pore Pressure and Pressure Gradient Distribution

Locations L1, L2, L3, L4 and L5 are investigated in Fig. 7.3.4 for the amplitude of total pore pressure p_{max} at various skirt lengths. An increase of skirt length results in decrease in both the amplitude and gradient of the pore pressure, leading to more severe soil liquefaction around the foundation. Wave diffraction causes the upstream side of the foundation to experience

higher pore pressure amplitude and gradient than the downstream side. The vertical gradient of p_{max} under the foundation center is relatively insignificant compared to the other locations.



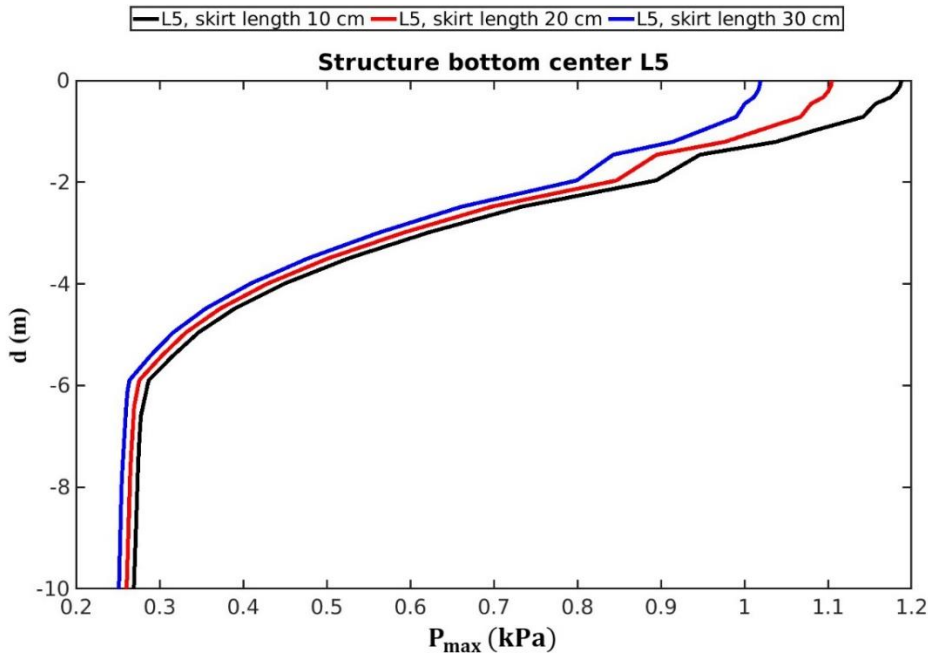
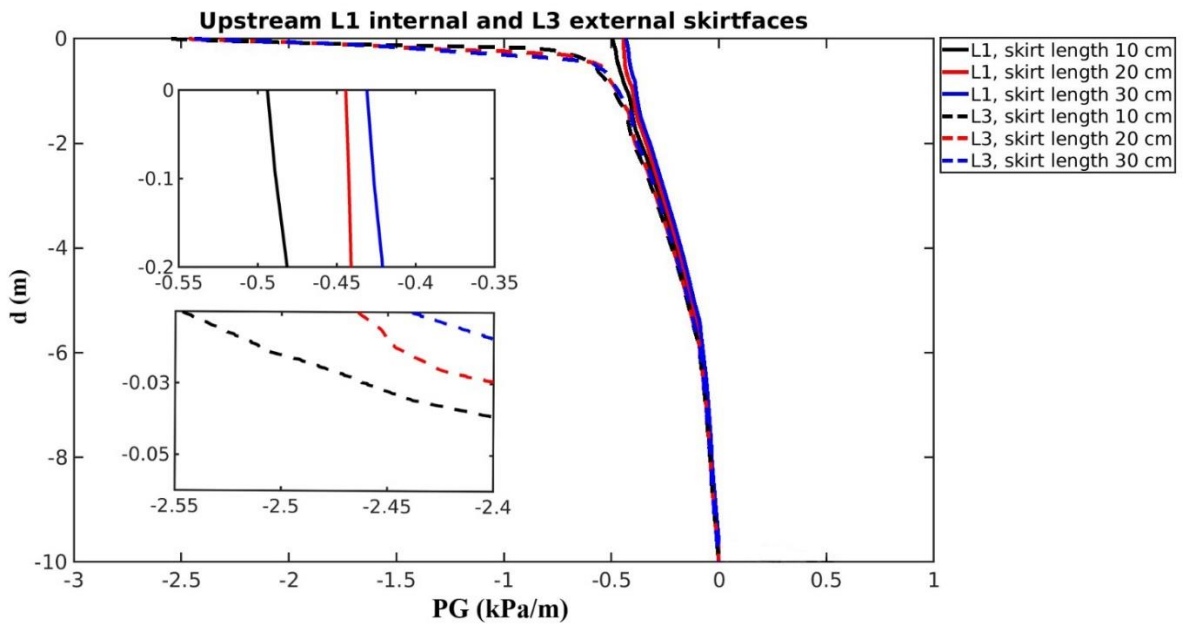


Figure 7.3.4 Vertical distributions of pore pressure amplitude p_{max} in various locations at different skirt lengths



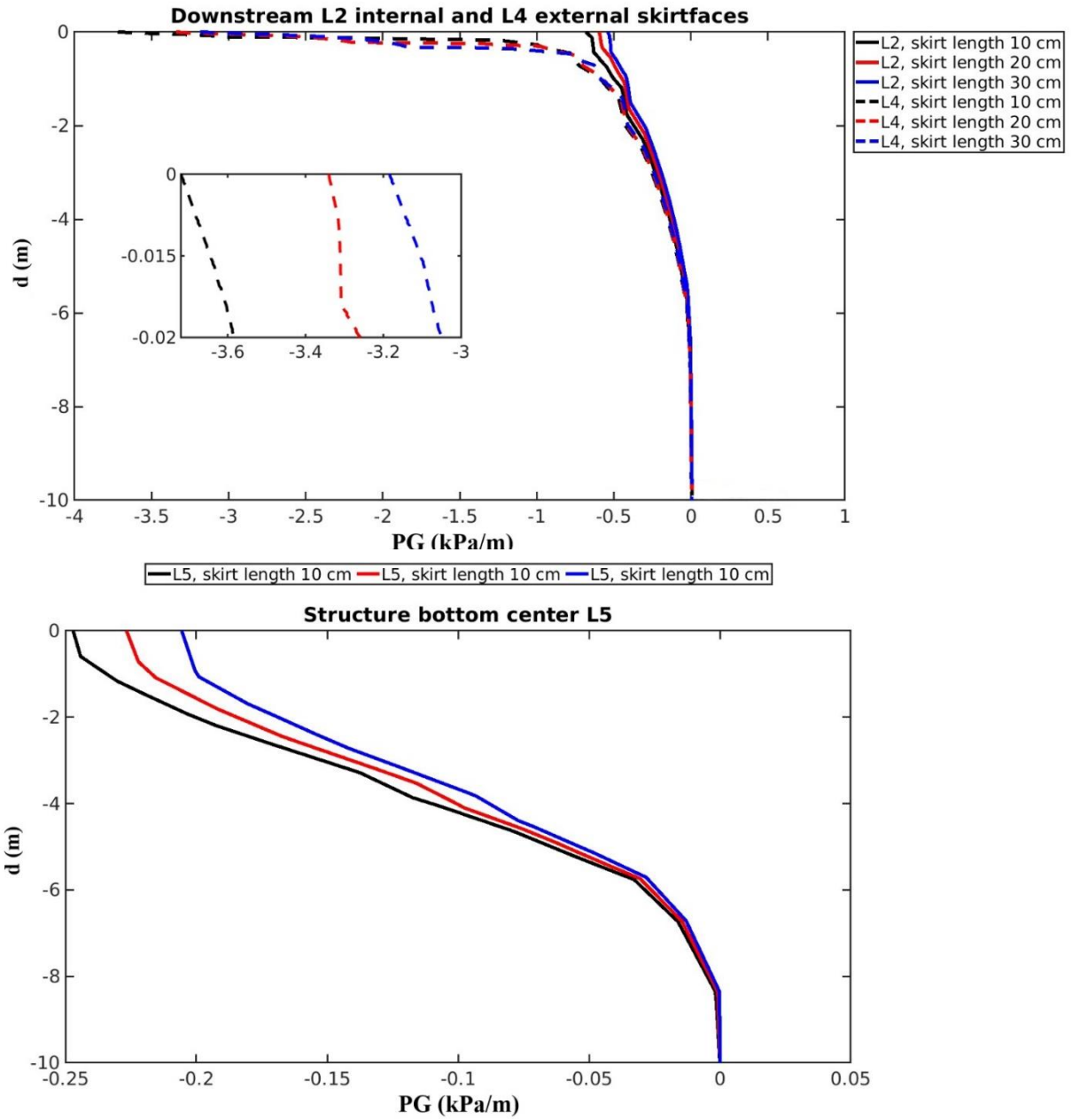


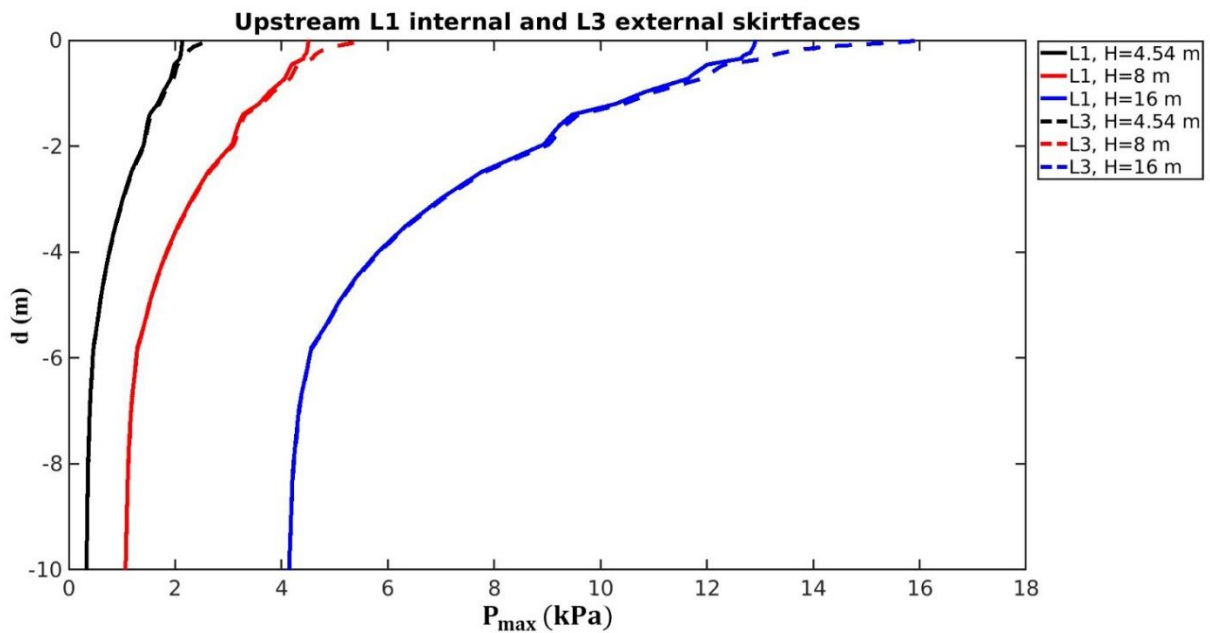
Figure 7.3.5 Vertical distributions of pressure gradient amplitude PG in various locations at different skirt lengths

7.4 Parameters comparison with different wave heights

In the previous paragraph, various parameters depending on the skirt length were considered. The greater the amplitude of pore pressure, the greater the likelihood of soil liquefaction. As can be seen from the graphs above, the largest range of parameters is in cases with a skirted GRP cover skirt length of 10 cm. Therefore, the case with a 10 cm skirt length is the most dangerous. The following comparison charts will be related to the case comparison of 10 cm skirt length at different wave heights between external and internal skirfases, structure bottom center.

Pore pressure distribution

In Figure 3.5.2, the amplitude of total pore pressure p_{max} at different wave heights was examined at five locations - L1, L2, L3, L4, and L5. An increase in wave height leads to an increase in the pore pressure amplitude, which can cause more severe soil liquefaction around the foundation. Wave diffraction causes the upstream side of the foundation to experience higher pore pressure amplitude and gradient compared to the downstream side.



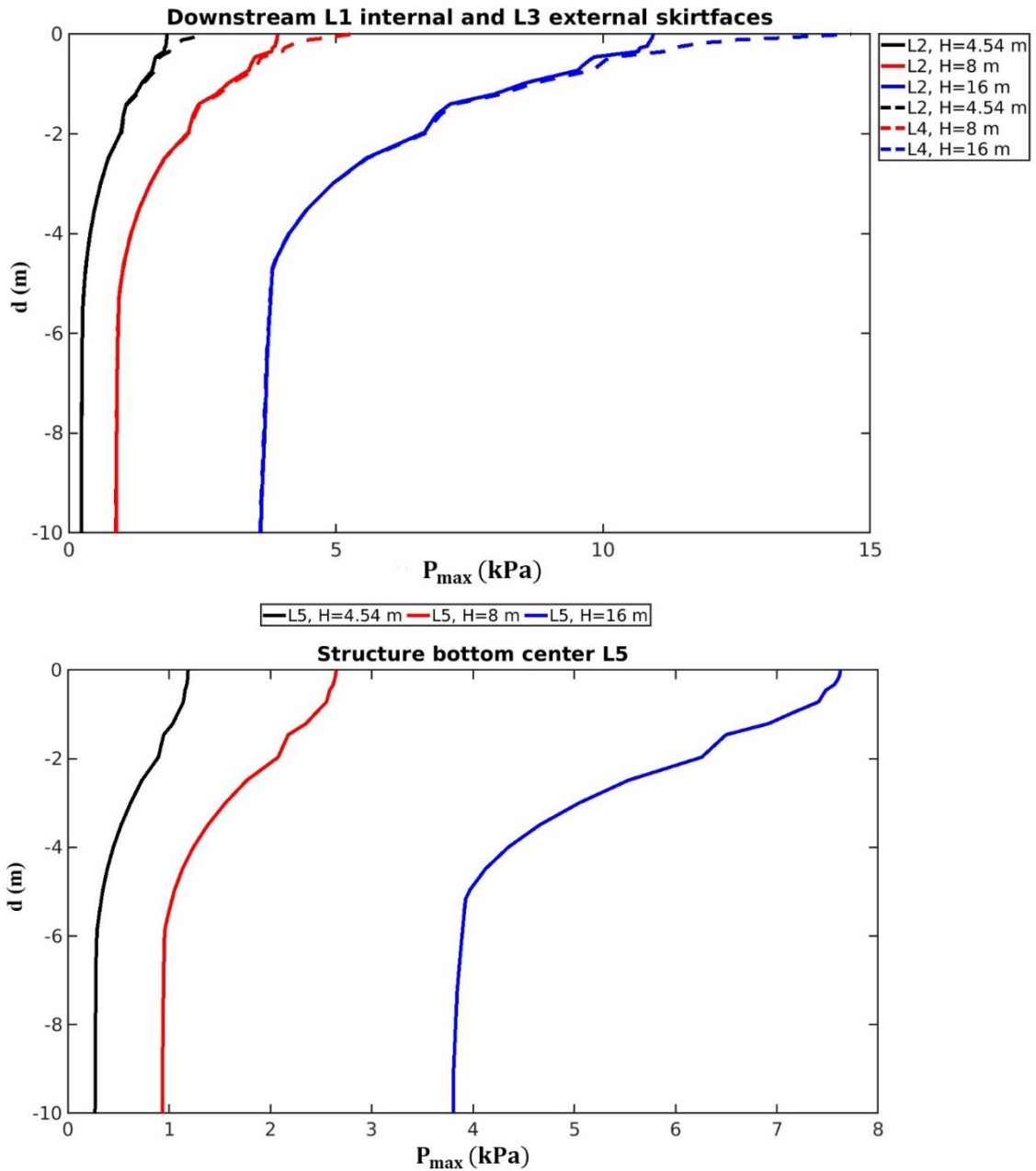


Figure 7.4.1 Vertical distributions of pore pressure amplitude p_{max} in various locations at different wave heights. Skirt length 10 cm

Vertical Displacement

Fig. 7.4.2 illustrates the maximum vertical soil displacement U_{Zmax} at different wave heights during a wave cycle, with the soil depth indicated by d (m). The results show that the vertical soil displacement increases with greater wave height. Furthermore, it is observed that internal skirt face locations L1 and L3 have larger amplitude than external skirt face areas L2 and L5. The figures below provide a comparison.

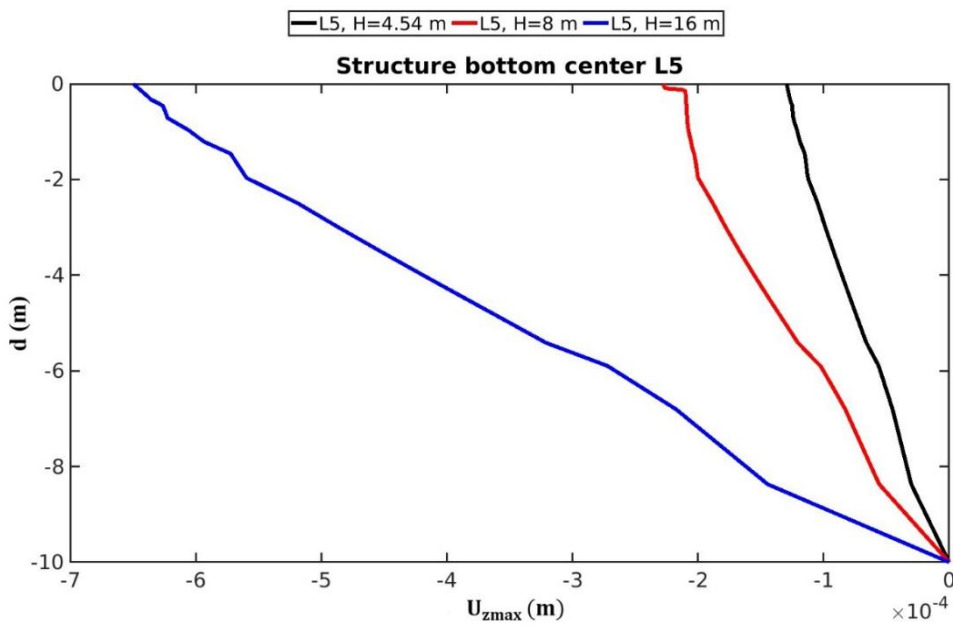
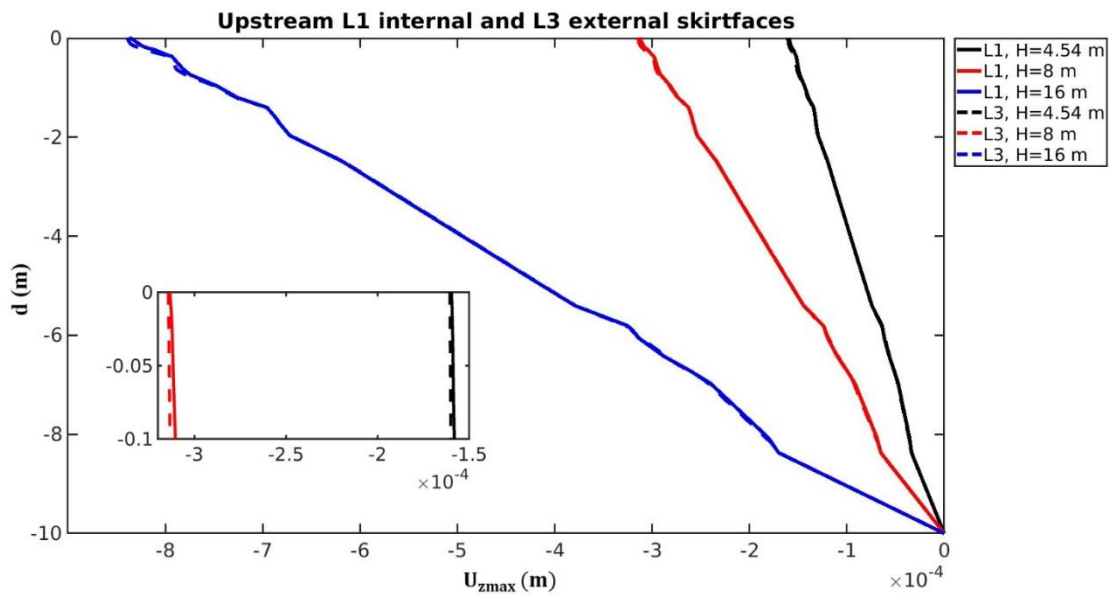
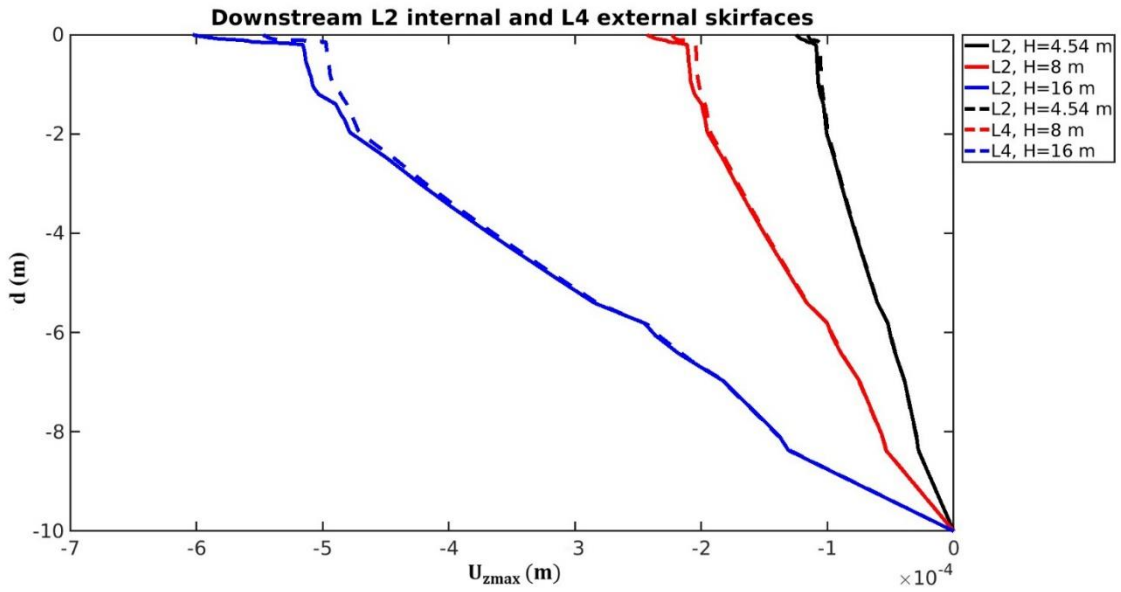
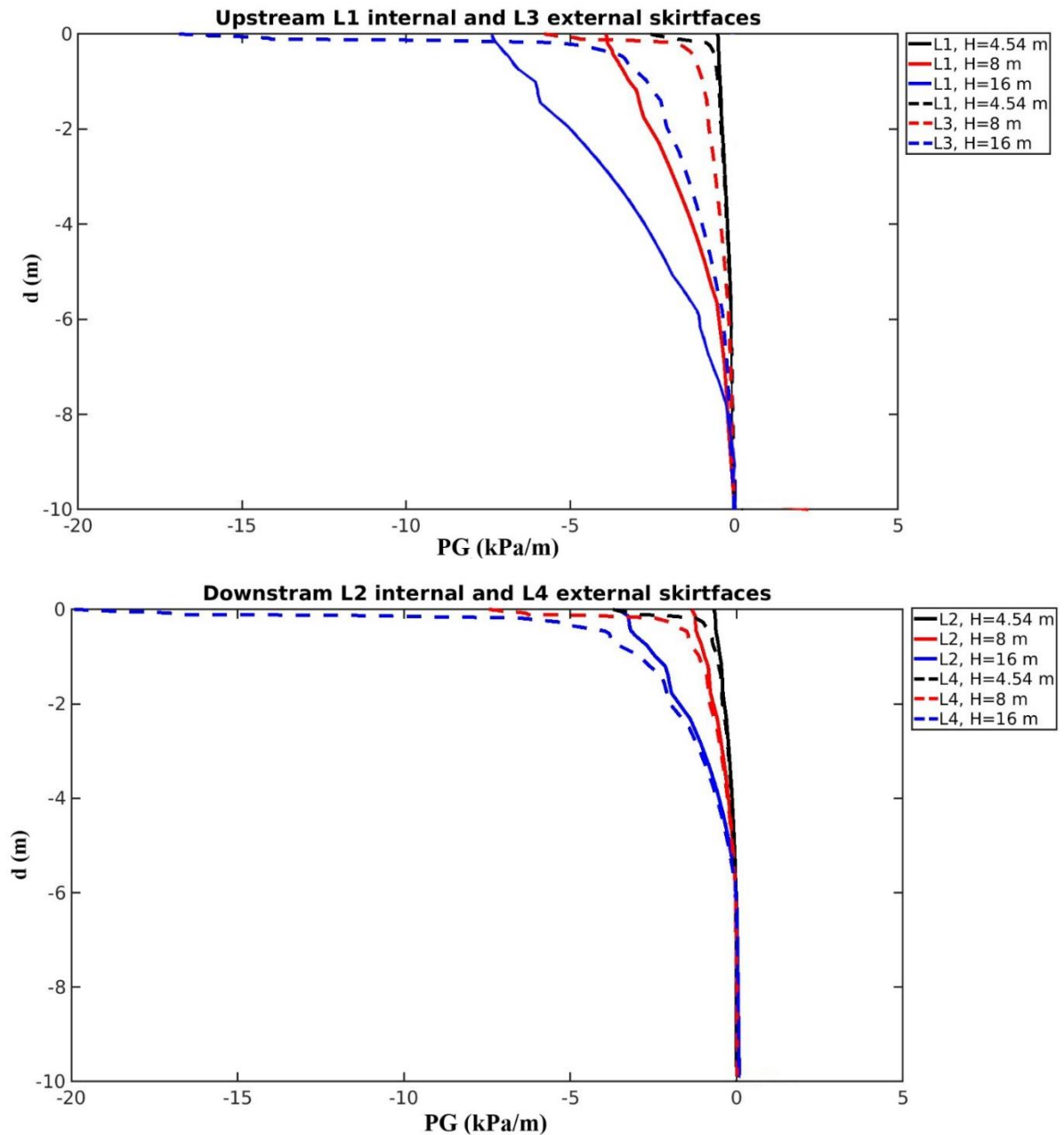


Figure 7.4.2 Vertical distributions of vertical displacement amplitude U_{Zmax} in various locations at different wave heights. Skirt length 10 cm

Pressure Gradient

Fig. 7.4.3 illustrates the maximum vertical soil displacement U_{Zmax} at different wave heights during a wave cycle, with the soil depth indicated by d (m). The results show that the vertical soil displacement increases with greater wave height. Furthermore, it is observed that internal skirt face locations L1 and L3 have larger amplitude than external skirt face areas L2 and L5. The figures below provide a comparison.



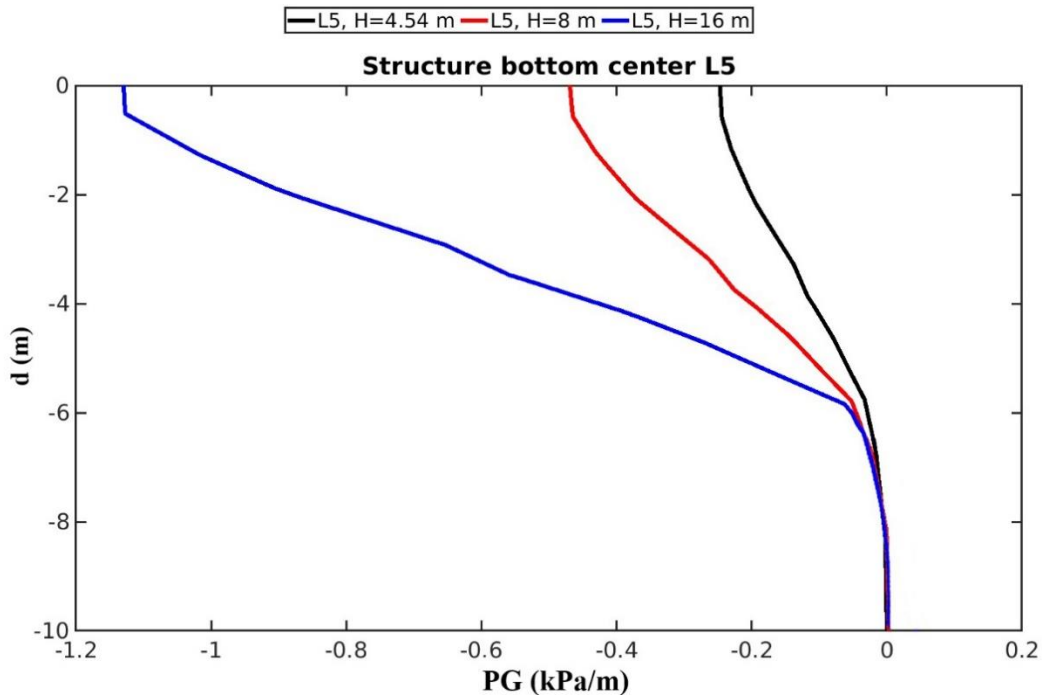


Figure 7.4.3 Vertical distributions of pressure gradient amplitude PG in various locations at different wave heights. Skirt length 10 cm

Lifting (F_z) and Drag (F_x) Forces

Figures 7.4.4 and 7.4.5 observe lifting and drag forces changings depends on various wave heights $H=1.94\text{m}$, $H=3.24\text{m}$, $H=4.54\text{m}$, $H=8\text{m}$ and $H=16\text{m}$. Each wave simulation had been run until 500 s. The most stabilized areas of the simulations were chosen for data extraction. The results show that the lifting and drag forces increase with greater wave height.

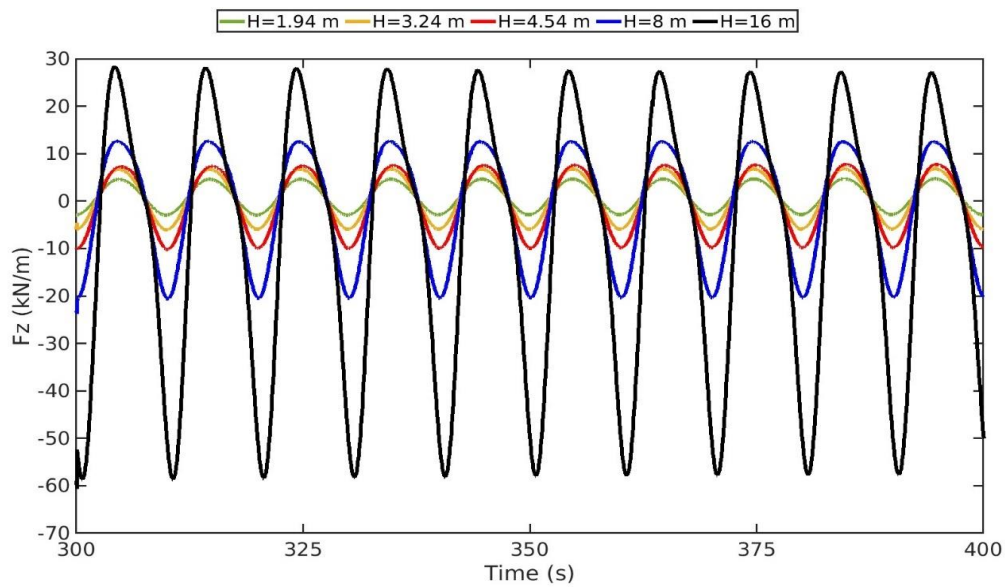


Figure 7.4.4 Wave induced Lifting force (F_z) depending on the wave heights

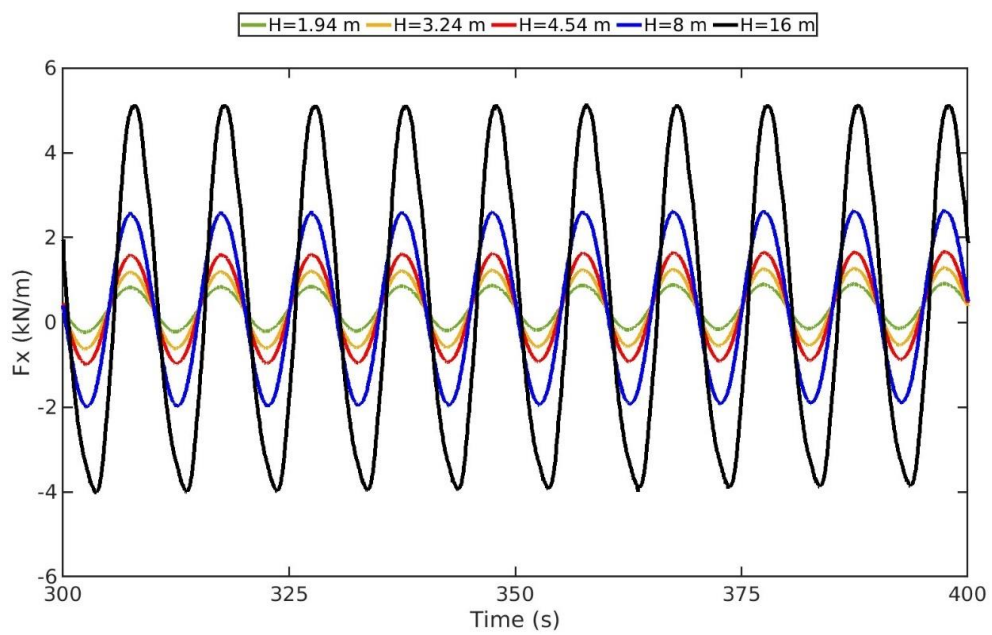


Figure 7.4.5 Wave induced Drag force (F_x) depending on the wave heights

When ocean waves propagate towards a submerged pipeline, they generate hydrodynamic forces that interact with the seabed. The seabed soil responds to these forces by deforming and generating pore pressure. This deformation and pore pressure, in turn, create a resistance force on the pipeline that opposes the wave-induced force. Figure 7.4.6 shows the delay between Lifting force (F_z) and Drag force (F_x) amplitudes in one wave length.

This interaction between the pipeline, seabed soil, and wave-induced forces leads to a delay in the amplitude of the lifting and drag forces acting on the subsea GRP cover. The delay is caused by the time taken for the wave-induced forces to propagate through the seabed soil, generate a resistance force, and then transmit this force to the pipeline. Additionally, the cover itself may also start to move due to the lifting forces, which can further affect the wave dynamics. The delay can affect the dynamic response of the cover, and hence its ability to protect subsea assets such as pipelines and cables.

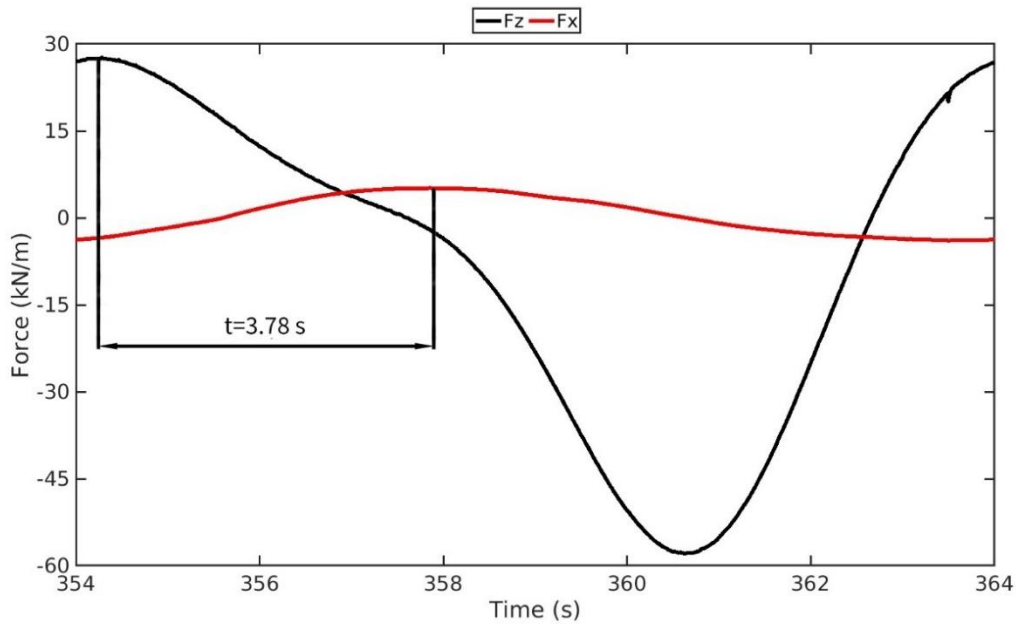


Figure 7.4.6 The delay between Lifting (F_z) and Drag (F_x) forces amplitudes in one wave length

7.5 Liquefaction Analysis

According to available literature, there have been multiple proposed liquefaction criteria to study momentary liquefaction, utilizing either effective stress (Tsai, 1995; Okusa, 1985) or excess pore pressure (Zen and Yamazaki, 1990; Jeng, 1997a). Ye (2012b) has carried out a comparative analysis of these liquefaction criteria. The present study utilizes a modified form of the excess pore pressure-based, one-dimensional liquefaction criterion proposed by Zen and Yamazaki (1990).

$$p - p_b \geq -(\gamma_s - \gamma_w)z \quad (26)$$

In the given equation, γ_s and γ_w represent the unit weight of soil and water, respectively, while p_b denotes the pore wave pressure at the seabed surface.

In the present study, considering the structure on the seabed, the momentary liquefaction is examined by:

$$p - p_b \geq \sigma'_{z0} \quad (27)$$

In the given equation, the initial vertical effective stress σ'_{z0} is included, which arises from the consolidation process under the influence of gravitational forces. This same criterion has been employed with favorable outcomes in the works of both Sui et al. (2017) and Zhao et al. (2017).

In previous sections it's been explained that the liquefaction risk increases with increasing the amplitude of pore pressure which depends on the wave height and skirt length respectively. Figures 3.6.1 and 3.6.2 represent the liquefaction value in 10 cm and 30 cm cases when the wave crest passes the construction. The greater the wave height, the larger dynamic pressure induces soil pore pressure, hence, 16 m wave height used as a critical case for further observation.

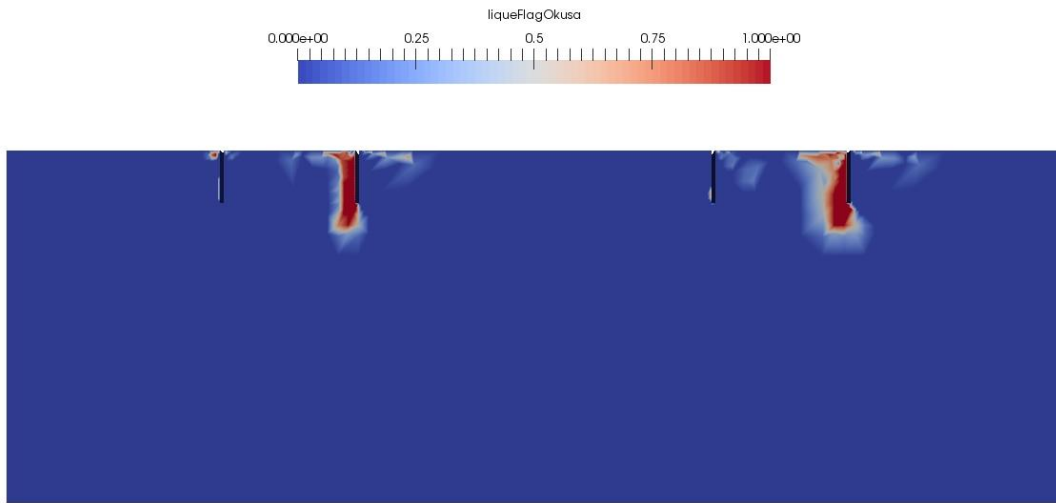


Figure 7.5.1 Liquefaction at the 30 cm skirt length when the wave crest passes the construction

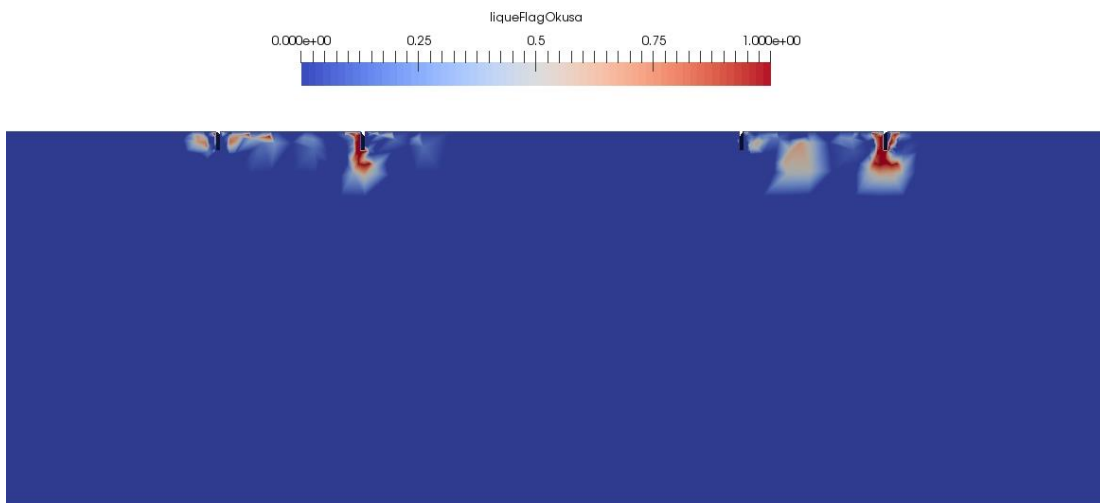


Figure 7.5.2 Liquefaction at the 10 cm skirt length when the wave crest passes the construction

Soil liquefaction depends and most likely occurs along the skirt length. Comparing these two figures it is noticeable that the liquefaction area in 10 cm skirt length case is larger than in 30 cm skirt length case. It is interesting that liquefaction area mostly takes place at the internal skirfaces areas. It depends on the excess pore pressure, that has actually larger value in 10 cm skirt length case.

8 Conclusions

In this study, the soil response and potential liquefaction caused by waves at the skirted GRP cover were investigated. A wave-structure-seabed interaction model based on 2D FVM was utilized. To ensure accuracy, numerical sub-models were subjected to grid convergence studies of several parameters including lifting (F_z) and drag (F_x) forces. The study involved the analysis of various parameters changing depend on skirt lengths and wave heights.

In summary, this study has led to the following conclusions:

- 1) The seabed soil experiences the greatest shear stress directly beneath skirts. The skirts presence on the seabed causes significant soil response changes by increasing the wave-induced shearing effect on the underlying seabed. Regions with high shear stress may be prone to local plastic failure.
- 2) The presence of the structure on the seabed leads to an increase in wave-induced vertical soil displacement in the surrounding area especially at the structure bottom center.
- 3) The soil beneath the structure bottom center has a smaller gradient of pore pressure than the soil underneath the skirts. The maximum values of the pressure gradient is located in the area closest to the internal skirfaces. That indicates that liquefaction is less probable to occur underneath the structure bottom center and more likely at the internal skirfaces areas.
- 4) The momentary liquefaction risk increases with higher wave height and lower skirt length due to the pore pressure value increasing.
- 5) The most severe liquefaction rates are at the moment when wave crest and wave trough are above the structure. When the wave crest is upcoming, liquefaction at the left skirt sides arise. When the wave trough is upcoming, liquefaction at the right skirt sides arise.

The present 2D wave-structure-seabed interaction model assumes the seabed soil behaves elastically, neglecting soil strength limitations and plastic deformation. Also, the seabed soil was taken as an isotropic. Moreover, 2D simulation doesn't reflect the full-scale situation. As a result, introducing a nonlinear soil model could produce different soil response outcomes. Further experimental data is necessary to validate the current numerical results. In the meantime, this method can be a practical engineering tool to forecast the wave-induced soil response near offshore foundations.

References

- Biot, M.A., 1941. General theory of three-dimensional consolidation. *J. Appl. Phys.* 12, 155–164
- Biot, M.A., 1956. Theory of propagation of elastic waves in a fluid-saturated porous solid. ii. higher frequency range. *J. Acoust. Soc. Am.* 28, 179–191
- Fenton, J.D., 1985. A fifth-order Stokes theory for steady waves. *J. Waterw. Port, Coast. Ocean Eng.* 111, 216–234.
- Jeng, D., Hsu, J., 1996. Wave-induced soil response in a nearly saturated sea-bed of finite thickness. *Geotechnique* 46, 427–440.
- Jeng, D.-S., 2012. *Porous Models for Wave-Seabed Interactions*. Springer Science & Business Media, pp. 13–17.
- Jeng, D.-S., Cha, D., 2003. Effects of dynamic soil behavior and wave non-linearity on the wave-induced pore pressure and effective stresses in porous seabed. *Ocean. Eng.* 30, 2065–2089.
- Jeng, D.-S., Lin, Y.-S., 2000. Poroelastic analysis of the wave–seabed interaction problem. *Comput. Geotech.* 26, 43–64.
- Jeng, D.-S., Rahman, M., 2001. Wave-induced oscillatory soil response: difference between quasi-static and dynamic solutions. *Computer Methods and Advances in Geomechanics* 2, 1103–1106.
- Jeng, D.-S., Ye, J.-H., Zhang, J.-S., Liu, P.-F., 2013. An integrated model for the wave-induced seabed response around marine structures: model verifications and applications. *Coast. Eng.* 72, 1–19.
- Li, Y., Ong, M.C., Tang, T., 2019. <https://github.com/liyzpearl/wssi>.
- Li, Y., Ong, M.C., Tang, T., 2018. Numerical analysis of wave-induced poro-elastic seabed response around a hexagonal gravity-based offshore foundation. *Coast. Eng.* 136, 81–95
- Li, Y., Ong, M.C., Tang, T., 2019. A numerical toolbox for wave-induced seabed response analysis around marine structures in the OpenFOAM® framework. *Coast. Eng.*
- Ong, M.C., Trygslund, E., Myrhaug, D., 2016. Numerical study of seabed boundary layer flow around monopile and gravity-based wind turbine foundations. In: *ASME 2016 35th International Conference on Ocean, Offshore and Arctic Engineering*, American Society of Mechanical Engineers. V002T08A011–V002T08A011